Super-collimation in a Rod-based Photonic Crystal

by

Ta-Ming Shih

B.S. Electrical Engineering and Computer Science
University of California, Berkeley 2006

Submitted to the Department of Electrical Engineering and Computer Science in partial fulfillment of the requirements for the degree of

Master of Science in Electrical Engineering

at the
MASSACHUSETTS INSTITUTE OF TECHNOLOGY

September 2007

Author .....
Ta-Ming Shih
Department of Electrical Engineering and Computer Science
August 20, 2007

Certified by .....
Leslie A. Kolodziejski
Professor of Electrical Engineering and Computer Science
Thesis Supervisor

Accepted by .....
Arthur C. Smith
Chair, Department Committee on Graduate Students

Super-collimation in a Rod-based Photonic Crystal

by

Ta-Ming Shih

Submitted to the Department of Electrical Engineering and Computer Science
on August 20, 2007, in partial fulfillment of the
requirements for the degree of
Master of Science in Electrical Engineering

Abstract

Super-collimation is the propagation of a light beam without spreading that occurs when the light beam is guided by the dispersion properties of a photonic crystal, rather than by defects in the photonic crystal. Super-collimation has many potential applications, the most straight-forward of which is in the area of integrated optical circuits, where super-collimation can be utilized for optical routing and optical logic. Another interesting direction is the burgeoning field of optofluidics, in which integrated biological or chemical sensors can be based on super-collimating structures.

The work presented in the thesis includes the design, fabrication, and characterization of a rod-based two-dimensional photonic crystal super-collimator. The dispersion contours for the photonic crystal are simulated as part of the design process. Two different fabrication process methods are developed and applied. The super-collimator is fabricated, and the fabrication methods are analyzed and compared. Characterization of the super-collimator has resulted in the first experimental observation of super-collimation in a two-dimensional photonic crystal of rods. The advantages of the rod-based device structure and potential applications of the super-collimator are discussed in closing.

Thesis Supervisor: Leslie A. Kolodziejski
Title: Professor of Electrical Engineering and Computer Science

Acknowledgments

The work I present here could not have been possible without the help and support of many people, and "Thank you" hardly does justice for the priceless experience of my first year at MIT.

First and foremost, I want to thank my advisor Professor Leslie Kolodziejski for her guidance. Her direction has made this past year for me very fruitful, and I am excited that I will have her for my advisor as I work towards a PhD. I want to thank her also for her humor, because often it is her optimism that has helped me keep my head above water.

I also must thank Dr. Gale Petrich for his mentorship and enthusiasm. He is always ready to put down what he is doing to answer any questions or discuss any topic with me. "If anything goes wrong, Gale can fix it."–That is my understanding, and I doubt anything will ever convince me otherwise.

I want to thank my colleagues involved in the super-collimation project: Marcus Dahlem, Andre Kurs, Dr. Katherine Hall, Dr. Morris Kesler, Professor Erich Ippen, and Professor Marin Soljačić. The collaboration was wonderful and I am extremely proud that we achieved the results we strived for.

A large part of my research was performed in the Nanostructures Laboratory (NSL) headed by Professors Henry Smith and Karl Berggren. At the NSL, James Daley has been a tremendous help with just about everything fabrication-related I can think of. Every time I speak with him, I learn something new. I also want to express my gratitude toward Dr. Timothy Savas, Ryan Williams, Hsin-Yu Tsai, Charles Holzwarth, Natalija Jovanovic, Bryan Cord, Joshua Leu, and Thomas O'Reilly. A special thanks goes to Orit Shamir for her help with the RIE.

Finally, I want to thank my mother and father for their love and care for me while I am 3000 miles away from home. I also want to thank my sister Hui-Wen, who has always been there for me. And lastly, a warm thank-you to Angela Zhou, who is everything I could ever ask for.

Cambridge, 2007 TM S

Contents

1 Introduction **17**

1.1 What Are Photonic Crystals? 18

1.2 Related Work 19

1.3 Thesis Organization 20

2 Theory, Simulation, and Design **21**

2.1 How Does Super-collimation Work? 21

2.2 Simulation Theory 24

2.3 Device Design and Simulation Results 28

2.4 Rod and Hole Sensitivities 29

3 Fabrication Approach **33**

3.1 Interference Lithography 34

3.1.1 Rod and Hole Pattern Definition 37

3.1.2 Sample Preparation 40

3.2 Lift-off Process Fabrication 43

3.2.1 Interference Lithography 43

3.2.2 Reactive Ion Etching 45

3.2.3 Lift-off 47

3.2.4 CF_4/O_2 Si-RIE 48

3.3 Main Process Fabrication 50

3.3.1 Interference Lithography 50

3.3.2 Reactive Ion Etching 52

3.3.3 Cl_2 Si-RIE 54
3.4 Device Statistics 58
3.5 Cleaving 63

4 Optical Characterization **65**
4.1 Measurement Apparatus 65
4.2 Results and Discussion 66

5 Conclusion **71**
5.1 Applications and Future Work 71

A Tables **75**

List of Figures

1-1 A 2D PhC of air-holes in contrast to a 2D PhC of rods. 17

1-2 Photonic crystals are dielectric structures whose dielectric constant exhibits periodicity in one, two, or three dimensions. 18

2-1 A laser beam spreads when propagating in free-space (left) but remains collimated for propagation in a 2D PhC (right). Every point on the same contour line is at the same frequency. 23

2-2 The 2D rod-based PhC that is designed to super-collimate at $\lambda = 1550$ nm. 28

2-3 Simulated equifrequency contours for a 2D rod-based PhC with a square lattice having lattice constant $a = 437.5$ nm, rod diameter $d = 250$ nm, and rod height $h = 700$ nm. Super-collimation is seen to occur at a wavelength close to $\lambda = 1550$ nm. 30

3-1 The 2D rod-based PhC that is designed to super-collimate at $\lambda = 1550$ nm. 33

3-2 IL involves the interference of two plane waves to create a standing wave pattern that is imaged into the photoresist. 34

3-3 The graph of Equation 3.3 with $A_1 = A_2 = 1$ and $p_1 = p_2 = 1$. 36

3-4 The Lloyd's Mirror IL set-up. The angle θ is set by turning the entire stage. 36

3-5 Far below (left) and above (right) the Crossover Dose, the photoresist holes and rods have circular cross-sections. A positive resist is assumed here, and lengths are in arbitrary units. 38

3-6 Near the Crossover Dose the photoresist holes (left) and rods (right) have square-shaped cross-sections. A positive resist is assumed here, and lengths are in arbitrary units. 38
3-7 A square-like shape is visible in the SiO_2 etchmask as imaged from the top of a finished Main Process device. The exposure time was 125 s at a laser power of 0.48 mW. 39
3-8 Near the edge of a large sample, the pattern in SiO_2 on SOI wafer of a Main Process sample consisted of a combination of rods and holes. Exposure was for 125 s at a laser power of 0.48 mW. 39
3-9 Sample preparation diagrams for the Lift-off Process (left) and the Main Process (right). Dimensions are not to scale. This is the state of the samples right before IL exposure. 41
3-10 Left: for the Lift-off Process, the simulation indicates that the back-reflection into the PR will be minimized if the ARC layer has a thickness of 296 nm, but the local minimum of a thickness of 400 nm was chosen to facilitate the lift-off step. Right: for the Main Process, the simulation indicates that the back-reflection into the PR will be minimized if the ARC layer has a thickness of 286 nm. 42
3-11 Developed PS4 photoresist on the SiO_2 interlayer: examples of monitor samples used to determine the correct exposure time for the pattern. The sample on the left was exposed for 15 s (in each orthogonal direction), and the sample on the right was exposed for 20 s (in each orthogonal direction). 43
3-12 Lift-off Process Flow (dimensions not to scale). 44
3-13 SiO_2/ARC holes on Si, prior to lift-off. 47
3-14 Cr rods on SOI wafer. The Cr rods shown here, which look more like mounds, are 120 nm high, instead of 150 nm used for the finished device. 48
3-15 The finished 2D rod-based PhC super-collimator fabricated with the Lift-off Process. In the SEM micrograph, the 3 μm of SiO_2 is clearly visible, due to the distinct manner that SiO_2 often cleaves. 49

3-16 The laser beam is coupled into the super-collimator at normal incidence. (a) The orientation of the pattern on the samples fabricated with the Lift-off Process did not allow light to be coupled into the super-collimator in the correct direction. (b) The orientation of the pattern for the Main Process samples were rotated 45° and allowed light to be coupled into the super-collimator in the correct (Γ-M) direction. 49

3-17 Main Process Flow (dimensions not to scale). 51

3-18 120-nm-high SiO_2 rods on a SOI wafer. The sample was a monitor sample that was exposed for 135 s in each direction (not 125 s as for the finished device). 53

3-19 Hollowed ARC shells after a Cl_2 reactive ion etch. The boundary between the BARLi and SiO_2 is not clearly defined in the image. . . . 53

3-20 Contamination in the RIE chamber caused micromasking and produced many tiny rods, leading to "grass" or "black silicon," which is observed in the right part of the image. The left part is a layer of hydrogen silsesquioxane (HSQ) which masks the Si, and therefore grass is not observed. The inset magnifies the boundary between the grass and HSQ. Small particulates on the HSQ can be observed and are speculated to be due to contamination in the chamber. It is unclear why there seems to be an area along the edge where there are no particulates. 54

3-21 A successful Cl_2 reactive ion etch of Si. Tapering is very noticeable in this sample, which was a monitor sample that was exposed for 135 s in each direction (not 125 s as for the finished device). 55

3-22 The result of an experiment to reduce the tapering. The sample was etched in Cl_2 for 5 minutes, removed from the RIE chamber for 1 hour, and then etched in Cl_2 for 5 more minutes. 56

3-23 The intensity profile of a mode in the super-collimated region, as viewed from the side (left) and from the top (right). The shape of the tapered rods, shown by the white lines, are superimposed. The simulation shows that the modes are well-confined to the plane of the slab, allowing super-collimation to occur in a device with tapered rods. 57

3-24 The finished 2D rod-based PhC super-collimator fabricated with the Main Process. In this SEM micrograph, the 3 μm of SiO_2 is clearly visible, due to the distinct manner that Si often cleaves. 57

3-25 Top-down view of a Lift-off Process device taken with the Raith 150 Scanning Electron Beam Lithography tool. The Cr etchmask has been removed to reveal the flat tops of the Si rods. The variation in the shapes of the rods and sidewall roughness can be seen clearly. 58

3-26 Histograms of diameters for a Lift-off Process sample before (left) and after (right) the lift-off process. 60

3-27 Histograms of diameters for a Lift-off Process super-collimator (left) and a Main Process super-collimator (right). 60

3-28 The corner of a finished Main Process device at the intersection of 2 cleaves. The rods near the cleaved edges have dislodged due to the nature of the cleaving process. 64

4-1 One of the device samples resting on its holder. The device size is approximately 2.5 mm by 5 mm. 66

4-2 Left: schematic of the camera and fiber positions relative to the super-collimator under optical characterization. Right: photograph of the optical measurement apparatus. 66

4-3 Super-collimation observed at a wavelength of $\lambda = 1545$ nm. The image is approximately 250 μm wide. 67

4-4 The divergence of the beam as a function of wavelength is seen clearly in the set of top-view IR images. Each image is approximately 125 μm wide. Super-collimation occurs close to $\lambda = 1530$ nm. 68

4-5 Demonstration of super-collimation for a distance of at least 350 μm at $\lambda = 1550$ nm. 69

5-1 In a 2D PhC of rods, fluid can flow parallel to the PhC plane between the rods. 72

5-2 A possible chemical sensor structure based on a Mach-Zehnder design utilizing super-collimating 2D PhCs of rods. 73

List of Tables

3.1 Estimated population standard deviation of feature diameters in units of pixels. 60

A.1 Refractive indices of relevant materials. 75

A.2 Spin-coating parameters 75

A.3 Lift-off Process RIE parameters 76

A.4 Main Process RIE parameters 76

A.5 “Outerlab” clean/condition process RIE parameters 76

Chapter 1

Introduction

Super-collimation is the propagation of a light beam without spreading that occurs when the light beam is guided by the dispersion properties of a photonic crystal (PhC), rather than by defects in the photonic crystal. Super-collimation has been previously shown theoretically and experimentally in two-dimensional (2D) PhCs of air-holes [1, 2]. The work presented in the thesis is the first experimental demonstration of super-collimation in a 2D PhC of rods. Figure 1-1 shows both types of 2D PhCs that have been used to investigate super-collimation. [1]

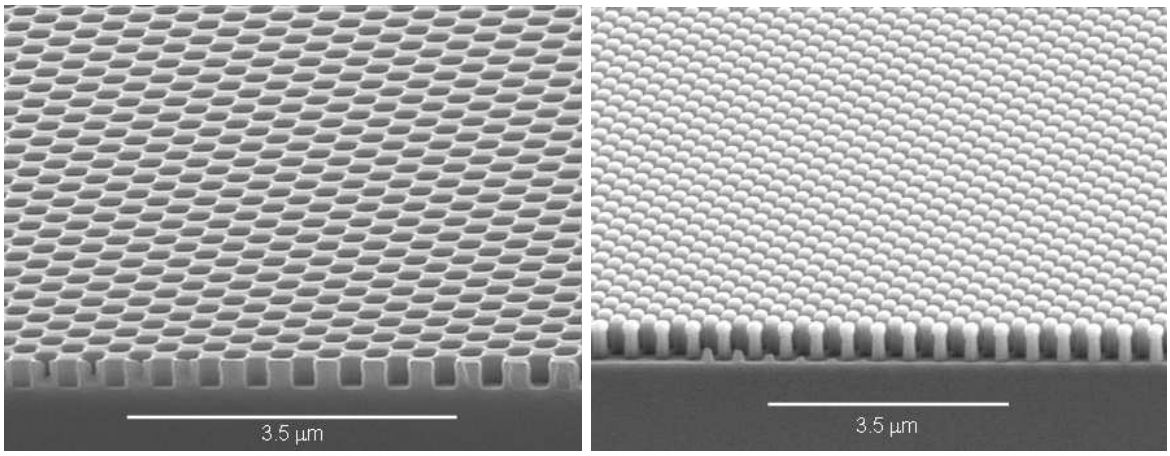

Figure 1-1: A 2D PhC of air-holes [1, 3] (left) in contrast to a 2D PhC of rods (right).

Super-collimation is an exciting phenomenon because it has many potential ap-

[1] All of the scanning electron microscope (SEM) images in the thesis were taken with the Zeiss 982 Gemini SEM.

plications. The most straight-forward application is in the area of integrated optical circuits, where super-collimation can be utilized for optical routing and optical logic [4]. Another interesting direction is the burgeoning field of optofluidics. In this area, rod-based super-collimators have certain advantages over holes, including an increased sensitivity to the ambient chemical composition, and good promise for decreased complexity of integration with microfluidics.

1.1 What Are Photonic Crystals?

Photonic crystals are dielectric structures whose dielectric constant exhibits periodicity in one, two, or three dimensions. They are called photonic "crystals", because their periodic structures resemble those of crystal lattices. Figure 1-2 is a schematic portraying different types of dielectric constant periodicity. Photonic crystals have many unique properties. One of the first properties predicted and experimentally verified was the existence of photonic band gaps, or frequency ranges for which the propagation of light in the photonic crystal is forbidden [5]. Hence, photonic crystals are often also called photonic band-gap (PBG) structures.

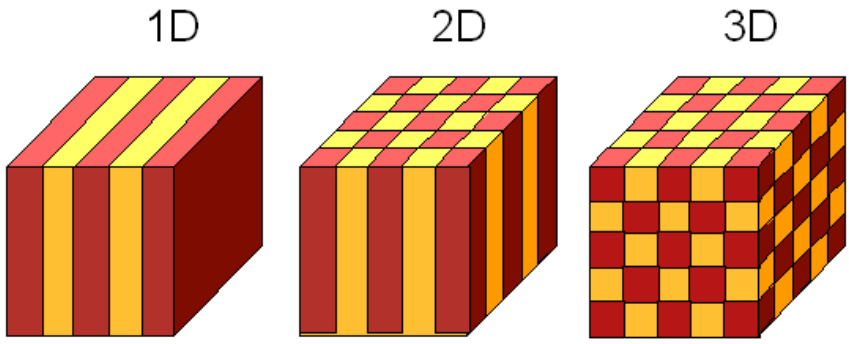

Figure 1-2: Photonic crystals are dielectric structures whose dielectric constant exhibits periodicity in one, two, or three dimensions. Diagrams adapted from [5].

More recently, photonic crystals have been shown to exhibit dispersion properties such as super-collimation and the superprism effect [6, 7]. The superprism effect occurs when a PhC behaves like an "amplified" prism. For small changes in the angle of

incidence of a monochromatic light beam into the superprism, large changes occur in the output angle. Furthermore, enhanced angular deflection is also seen for changes in the input wavelength. In contrast, super-collimation only occurs at a specific wavelength. Both the superprism effect and super-collimation are dispersion properties, which arise from the periodicity of the PhC. The theory behind dispersion phenomena will be discussed in Section 2.1. But first, a brief history of super-collimation is covered.

1.2 Related Work

The earliest demonstration of super-collimation, also termed self-collimation, was achieved by H. Kosaka and colleagues at NEC in Japan in 1999 [8]. Kosaka et. al. were able to demonstrate super-collimation theoretically and experimentally for a 3D PhC. Their super-collimating 3D PhC was fabricated in a planar fashion by depositing alternating layers of SiO_2 and amorphous Si via bias sputtering [9]. The vertical lattice constant was 320 nm and the lateral lattice constant was 330 nm. They demonstrated super-collimation for TM-polarized light at a wavelength $\lambda = 956$ nm.

T. Krauss' group at the University of St. Andrews, U.K., were the first to demonstrate super-collimation in a 2D PhC in 2003 [2]. The PhC was composed of a GaAs/AlGaAs heterostructure with a triangular lattice of air-holes having a lattice constant $a = 320$ nm and a hole diameter $d = 213$ nm. Super-collimation was observed for TE-polarized light with wavelengths λ from 1285 nm to 1310 nm. In 2D super-collimators, the light is confined in-plane by super-collimation, i.e. the PhC structure, and confined out-of-plane by total internal reflection within the slab.

Not long afterward, creative methods for routing super-collimated beams were developed. A former researcher at MIT, S. Fan, who is now at Stanford University, designed and simulated mirrors and splitters by using air-trenches in a 2D PhC of air-holes [10]. The square lattice of air-holes were in a material with dielectric constant $\epsilon_r = 12$, lattice constant a, hole diameter $d = 0.7a$, and super-collimated for TE-polarized light at a frequency of $0.19(c/a)$. At the University of Delaware, D. Prather's

group experimentally demonstrated beam-bending with mirrors [11]. Their super-collimator was a 2D PhC with a square lattice ($a = 442$ nm) of air-holes with diameter $d = 266$ nm, fabricated in the top silicon layer of a silicon-on-insulator (SOI) wafer. Reflection from the mirror was measured with a super-collimated beam at $\lambda = 1432$ nm. Prather's group also went on to design, among other things, what they call an analog-to-digital converter, and a reconfigurable optical switch for super-collimated beams [4].

In 2006, a collaborative effort at MIT between the groups of L. Kolodziejski, J. Joannopoulos, and E. Ippen successfully demonstrated super-collimation over 600 isotropic diffraction-lengths (8 mm) [1]. This is the longest measured super-collimated beam to date. The super-collimator was a large-area 2D PhC with a square lattice of air-holes (pictured in Figure 1-1, left). The lattice constant was 350 nm and hole diameter was 210 nm. The device was fabricated in the top Si layer (205-nm thick) of an SOI wafer. Super-collimation was observed for TE light at $\lambda = 1500$ nm. The work presented in the thesis is a continuation of this project. Instead of holes, the inverse structure of rods is investigated. The thesis discusses the theory, design, fabrication, and characterization of the rod-based device shown in Figure 1-1, right. This 2D PhC of rods is the first of its kind to successfully achieve super-collimation.

1.3 Thesis Organization

Chapter two describes the theory behind super-collimation and the mathematics of PhC band-structure simulations that are used in the design of the super-collimator.

Chapter three examines interference lithography as applied to the fabrication of 2D PhCs, and then goes into detail about the fabrication of the 2D PhC of rods.

Chapter four reports upon the optical characterization apparatus and the results obtained. The experimental observations are compared with the theoretical simulation results.

Chapter five concludes the thesis with discussions of applications and future work.

Chapter 2

Theory, Simulation, and Design

Light can be guided in a PhC in one of two methods. The first achieves waveguiding through the use of defects within the PhC, while the second method, super-collimation, uses the dispersion properties of the PhC. In the first method, the guided modes have frequencies that are within the photonic band-gap of the PhC. When defects are introduced into the PhC, confined states that lie within the band-gap are created, allowing waveguiding to be accomplished [12]. Viewed from another perspective, waveguiding occurs because light with a frequency in the photonic band-gap must remain confined to the defects, since the frequency of light is forbidden in the PhC. Super-collimation, on the other hand, occurs in a perfectly periodic photonic crystal, without defects. Light is guided by the dispersion properties of the PhC, which arise from its periodicity.

2.1 How Does Super-collimation Work?

The dispersion relation for any system describes how the wave-vector and frequency for plane waves are related. The dispersion relation describes all of the waves in the system because any wave can be constructed from a superposition of plane waves. For example, the well-known phonon dispersion relation studied in solid state physics describes the relationship between the oscillation of individual atoms (frequency) and their phase relationship with the surrounding atoms (wave-vector). Similarly, PhCs

have "photon" dispersion relations. A PhC is periodic, thus allowing its structure to be described by the same theory of Bravais lattices that is used to characterize crystals. For any photonic crystal, then, its reciprocal lattice can be determined. For a PhC whose lattice structure is two-dimensional, its reciprocal lattice is also two-dimensional. The dispersion relations are functions of position in this 2D reciprocal space. If graphed, each dispersion relation is a surface, so a top-view contour plot can be generated, much like the topographic maps used in geography. Every point on the same contour line has the same frequency, analogous to a topographical map, in which every point on the same contour line is at the same elevation. The dispersion relations are also referred to as the band structure, as well as dispersion surfaces, curves, or contours. In general, any photonic crystal has an infinite number of dispersion surfaces. Often, the lowest-frequency dispersion surface, also called the first band, is the one designed to exhibit super-collimation.

In free space, plane-wave propagation is isotropic and linear with the following dispersion relation:

$$\omega = c|\overline{k}| \tag{2.1}$$

where c is the speed of light, ω is the frequency in rad/s, and $\overline{k}$ is the wave-vector.

The propagation of electromagnetic energy for a plane wave is not given by the wave-vector $\overline{k}$, however, but by the group velocity $\overline{v}_g$. In 2D, the group velocity is defined as

$$\overline{v}_g = \hat{x}\frac{d\omega}{dk_x} + \hat{y}\frac{d\omega}{dk_y} \tag{2.2}$$

The group velocity is the 2D gradient of the dispersion plot. Recall that the direction of the gradient is always in the direction of fastest increase. On a 2D equifrequency contour plot, this translates to the following important fact: The direction of the group velocity for a particular k-vector is always perpendicular to the contour line at that position in k-space.

For example, in 2D free space, the dispersion surface is an upside down cone with

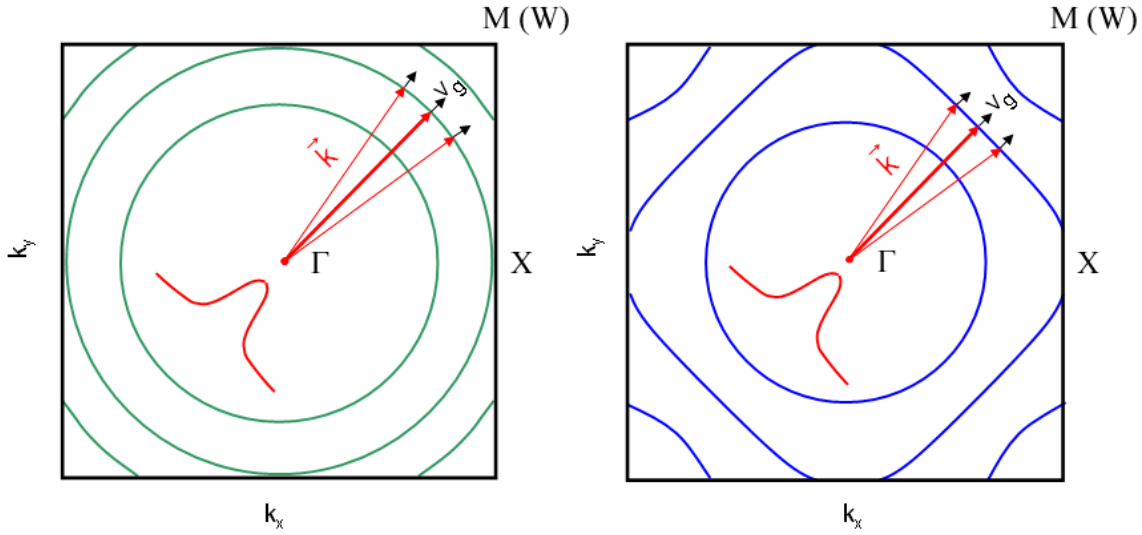

Figure 2-1: A laser beam spreads when propagating in free-space (left) but remains collimated for propagation in a 2D PhC (right). Every point on the same contour line is at the same frequency.

the apex at the origin. Therefore the equifrequency contours are concentric rings, as depicted in Figure 2-1, left. The energy of each plane wave travels in the direction perpendicular to the contour line. By observation, the direction of the group velocity $\overline{v}_g$ is in the same direction as the wave-vector, $\overline{k}$. In free space, the group velocity $\overline{v}_g$ equals the phase velocity $\overline{v}_p = c\hat{k}$. Recall that a single-wavelength laser beam is a superposition of a distribution of plane waves at the same frequency, centered around a certain wave-vector. The propagation direction is the direction of the central wave-vector. Suppose the laser beam is propagating at a 45° angle, or along the Γ-M direction, as shown in Figure 2-1, left. The group velocity $\overline{v}_g$ for each plane wave in the distribution points in a slightly different direction, causing the laser beam to spread.

In a 2D PhC, however, the dispersion curves can be engineered to have shapes other than a cone. In particular, a 2D PhC with a square lattice will often have a first-band dispersion contour plot as shown in Figure 2-1, right. The flat portion of the 2D PhC dispersion contour is what gives rise to super-collimation. Suppose the laser beam is propagating at a 45° angle, or along the Γ-M direction, inside the PhC as

shown. If the contour is flat, all of the plane waves in the distribution will have group velocities $\overline{v}_g$ in the same direction. The group velocity defines the energy propagation, which is no longer in the same direction as the phase. Instead, the group velocities are parallel, indicating that all of the energy travels in the propagation direction, resulting in super-collimation. In general, for 2D, whenever a contour line has a flat section, the PhC is capable of super-collimation for that frequency.

2.2 Simulation Theory

In the course of designing a device, the ability to verify that a certain design works is important to have. The dispersion properties of a PhC can be obtained through simulations. For the case of the super-collimator, calculations of the dispersion curves for a particular photonic crystal design are used to determine whether a contour line for the wavelength of interest has a flat region.

In solid state physics, the phonon dispersion curves for a crystal lattice is calculated by first developing a model of the lattice such that a wave equation can be determined. An area of research today is to develop more complex models for calculating better phonon dispersion curves. In the case of "photon" dispersion curves, there is no need to develop a model, since the Maxwell's equations already describe electromagnetic waves in a PhC.

The rest of this section is a brief overview of how the band structure is calculated in simulation software such as MIT Photonic Bands, which was used for the simulations in this project. For a more in-depth discussion please refer to [5, 13, 14, 15].

The source-free Maxwell's equations in SI units are

$$\nabla \cdot \overline{H}(\overline{r},t) = 0 \tag{2.3}$$

$$\nabla \cdot \epsilon(\overline{r})\overline{E}(\overline{r},t) = 0 \tag{2.4}$$

$$\nabla \times \overline{E}(\overline{r},t) = -\mu(\overline{r})\frac{\partial \overline{H}(\overline{r},t)}{\partial t} \tag{2.5}$$

$$\nabla \times \overline{H}(\overline{r},t) \;=\; \epsilon(\overline{r})\frac{\partial \overline{E}(\overline{r},t)}{\partial t} \tag{2.6}$$

where $\overline{H}$ is the magnetic field, $\overline{E}$ is the electric field, $\overline{r}$ is the position vector, t is time, ϵ is the permittivity, and μ is the permeability. The permeability for most dielectric materials is very close to the permeability of free space, μ_o, so the approximation $\mu = \mu_o$ will be made. A photonic crystal is then completely described by its permittivity function over space, $\epsilon(\overline{r})$. Recall that permittivity ϵ and dielectric constant ϵ_r are related by the permittivity of free space: $\epsilon = \epsilon_o\epsilon_r$. The index of refraction n is equal to the square-root of the dielectric constant, $\sqrt{\epsilon_r}$, to a good approximation for most materials. The permittivity, dielectric constant, and index of refraction are often used interchangeably.

The construction will be for harmonic modes of the electric field and the magnetic field. The reader should keep in mind that the solutions of harmonic modes can be superimposed to form any arbitrary electric and magnetic field distribution. In particular, the harmonic mode of the magnetic field has the form,

$$\overline{H}(\overline{r},t) = \overline{H}(\overline{r})e^{i\omega t} \tag{2.7}$$

in which the space and time dependencies of the H-field have been separated. This is analogous to the separation of space and time dependencies by which the time-independent Shrödinger equation is obtained from the time-dependent Shrödinger equation.

In the literature, the derivation to follow is most often performed with source-free Maxwell's equations in cgs units, rather than SI units. For the sake of following this standard, the derivation will be presented here in cgs units. The source-free Maxwell's equations in cgs units are

$$\nabla\cdot \overline{H}(\overline{r},t) \;=\; 0 \tag{2.8}$$

$$\nabla\cdot \epsilon(\overline{r})\overline{E}(\overline{r},t) \;=\; 0 \tag{2.9}$$

$$\nabla \times \overline{E}(\overline{r},t) = -\frac{1}{c}\frac{\partial \overline{H}(\overline{r},t)}{\partial t} \tag{2.10}$$

$$\nabla \times \overline{H}(\overline{r},t) = \frac{\epsilon(\overline{r})}{c}\frac{\partial \overline{E}(\overline{r},t)}{\partial t} \tag{2.11}$$

where c is the speed of light. The harmonic form of $\overline{H}(\overline{r},t)$ and $\overline{E}(\overline{r},t)$ can be substituted into Equations 2.10 and 2.11 to obtain

$$\nabla \times \overline{E}(\overline{r},t) = -\frac{i\omega}{c}\overline{H}(\overline{r},t) \tag{2.12}$$

$$\nabla \times \overline{H}(\overline{r},t) = \frac{i\omega\epsilon(r)}{c}\overline{E}(\overline{r},t) \tag{2.13}$$

Taking the curl of Equation 2.13 and substituting it into Equation 2.12, the master equation is derived, after the time dependence cancels out:

$$\nabla \times \left(\frac{1}{\epsilon(\overline{r})}\nabla \times \overline{H}(\overline{r})\right) = \left(\frac{\omega}{c}\right)^2 \overline{H}(\overline{r}) \tag{2.14}$$

The eigenvalue equation above, along with Equation 2.8, completely determines $\overline{H}(\overline{r})$. However, the Equation 2.14 is a very difficult differential equation to solve. In order to make the problem tractable, the differential equation is simplified into a matrix eigenvalue equation. To do this, one of the major theorems of solid state physics, Bloch's Theorem, is applied. Bloch's Theorem states that $\overline{H}(\overline{r})$ must be periodic with the periodicity of $\epsilon(\overline{r})$. This makes intuitive sense from a symmetry point of view.

Knowing that $\overline{H}(\overline{r})$ is periodic, Fourier analysis indicates that $\overline{H}(\overline{r})$ can be written as a sum of plane waves, which are indexed by $\overline{k}$.

$$\overline{H}(\overline{r}) = \sum_{\mu}\sum_{\overline{G}} h_{\overline{G},\mu}\hat{e}_{\mu}e^{i(\overline{k}+\overline{G})\cdot\overline{r}} \tag{2.15}$$

The vectors $\overline{G}$ are the reciprocal lattice vectors, $\hat{e}_{\mu}$ is a unit vector determined by the polarization μ, and $h_{\overline{G},\mu}$ are the Fourier Series coefficients for a particular $\overline{G}$ and μ. In a 2D PhC, the transverse electric (TE) modes have E-field parallel to the 2D

plane, and transverse magnetic (TM) modes have E-field perpendicular to the plane. Because the two polarizations are orthogonal, the polarizations can be considered independently.

$$\overline{H}(\overline{r}) = \sum_{\overline{G}} h_{\overline{G},TE}\hat{e}_{TE}e^{i(\overline{k}+\overline{G})\cdot\overline{r}} + \sum_{\overline{G}} h_{\overline{G},TM}\hat{e}_{TM}e^{i(\overline{k}+\overline{G})\cdot\overline{r}} \tag{2.16}$$

When the two polarizations are considered separately, the simulation can be executed twice, once for TE and once for TM. Any form of $\overline{H}(\overline{r})$ can be written as a superposition of TE and TM modes. If $\overline{H}(\overline{r})$ of a single polarization from Equation 2.16 is substituted into Equation 2.14, an eigenvalue matrix equation is obtained (Equation 2.17) [15].

$$\mathbf{H}(\overline{k}) \cdot \mathbf{h} = \left(\frac{\omega}{c}\right)^2 \mathbf{h} \tag{2.17}$$

where $\mathbf{H}$ is a matrix and $\mathbf{h}$ is a vector. The polarization μ has been left out, because it is assumed that a certain polarization has been selected. The elements in $\mathbf{h}$ are the Fourier Series coefficients $h_{\overline{G}}$ indexed by reciprocal lattice vectors, $\overline{G}$. The elements in $\mathbf{H}(\overline{k})$ are functions of $\overline{k}$, defined by Equation 2.18, where ε is the Fourier transform of ϵ.

$$H_{\overline{G},\overline{G}'} = |\overline{k} + \overline{G}||\overline{k} + \overline{G}'|\varepsilon^{-1}(\overline{G} - \overline{G}') \tag{2.18}$$

In practice, to calculate ε, ϵ is discretized and Fast Fourier Transform (FFT) methods are utilized. However, there is still a slight problem: Equation 2.17 is an infinitely large matrix equation! The natural thing to do is to truncate the matrix and solve a finite matrix equation. The number of plane waves taken into account can be on the order of thousands, meaning that $\mathbf{H}(\overline{k})$ is an $N \times N$ matrix, where N on the order of 10^3.

As an example, the steps in a dispersion relation calculation is detailed here. An arbitrary PhC is defined by its periodic permittivity function $\epsilon(\overline{r})$. First, a value for N is chosen, indicating the number of plane waves, or reciprocal lattice vectors $\overline{G}$, to take

into account. N should also be the number of grid points used in the discretization of $\epsilon(\overline{r})$ [15]. Next, the k-points of interest are chosen. Often, the band structure for a number of points in the irreducible Brillouin zone is calculated, from which the band structure for the entire reciprocal space can be found using symmetry. For each value of $\overline{k}$, the matrix $\mathbf{H}(\overline{k})$ is determined, which involves calculating ε, as mentioned above. Upon diagonalization of $\mathbf{H}(\overline{k})$, the N eigenvalues $\left(\frac{\omega}{c}\right)^2$, and therefore the N values of ω, are determined. This calculation is repeated for each value of $\overline{k}$ of interest. Finally, the values of ω at several $\overline{k}$s are "connected" to form the dispersion surfaces. The eigenvectors can be used to find the actual modes $\overline{H}(\overline{r})$ via Equation 2.15.

2.3 Device Design and Simulation Results

The super-collimating rod-based 2D PhC design is depicted in Figure 2-2.

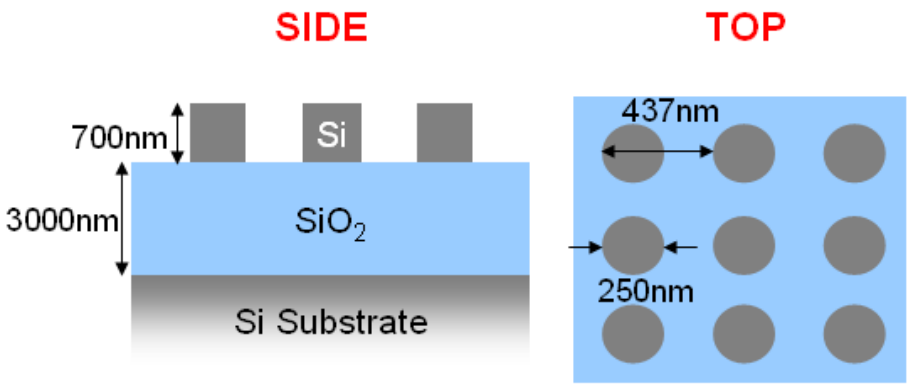

Figure 2-2: The 2D rod-based PhC that is designed to super-collimate at $\lambda = 1550$ nm.

The super-collimating wavelength was targeted to be somewhere in the optical telecommunications wavelength range (1260 nm - 1675 nm). This range is divided into many bands, or wavelength ranges. In particular, most of the telecommunications work has been done in the C-band (1530 nm - 1565 nm). The super-collimator was designed for a wavelength of 1550 nm, in the middle of the C-band.

Another constraint was posed by the wafer that was used to fabricate the device. Recall that in a 2D PhC super-collimator, the light is confined in-plane via super-

collimation, and out-of-plane via index guiding, or total internal reflection. Hence, the PhC must be isolated above and below by low-index material. For fabrication simplicity, a silicon-on-insulator (SOI) wafer was used. A typical SOI wafer consists of a thin top silicon layer above a thicker SiO_2 layer that resides on a thick Si substrate. SOI technology was first introduced as a way to improve circuit speed with better electrical isolation of transistors. For the purposes of this project, SOI is used for optical isolation of the PhC. Light is guided vertically in the top silicon layer because the light experiences low index material above (air; $n = 1.0$) and below (SiO_2; $n = 1.5$).

The SOI wafer that was available consisted of a 700-nm-thick top silicon layer and a 3-μm-thick oxide layer. For this reason the rods were designed to be 700 nm in height. Simulations were carried out with the MIT Photonic Bands software. A rod diameter of $d = 250$ nm and lattice constant of $a = 437.5$ nm (square lattice) was shown to exhibit super-collimation at $\lambda = 1550$ nm. Simulations also indicated that the 3 μm of oxide was sufficiently thick to confine the mode vertically. The refractive indices used for Si and SiO_2 were 3.52 and 1.53 respectively (at 1500 nm) [16]. The simulation results are shown in Figure 2-3.

2.4 Rod and Hole Sensitivities

One of the differences between rod-based and hole-based super-collimators is the spatial distribution of energy of a mode. For both types of super-collimators, the majority of the energy is contained in the higher index medium, in this case, silicon. However, in the case of rod-based super-collimators, a larger fraction of the energy is contained in the space outside of the silicon, and this fraction is proportional to the sensitivity of the device to a change in the ambient refractive index.

One way to characterize the sensitivity is to use a Mach-Zehnder interferometer in which each arm is a super-collimator. One super-collimator arm is contained in vacuum, while the other is immersed in a gas or liquid. The change in refractive index δn between the arms causes a change in the super-collimation frequency $\delta\omega$, which,

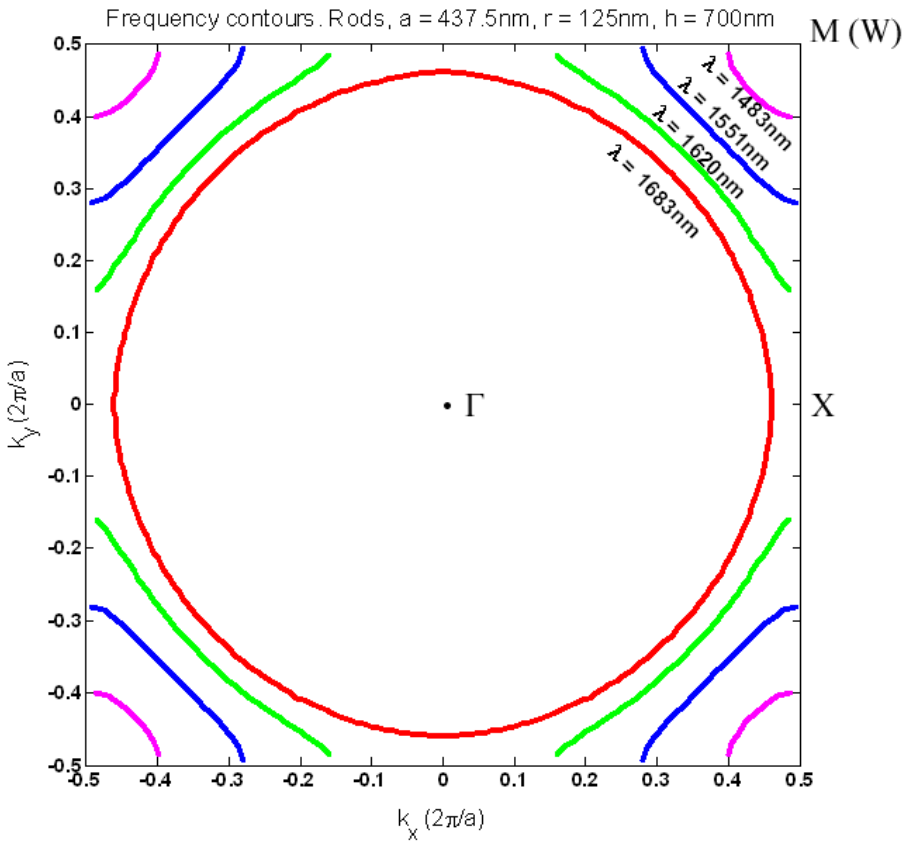

Figure 2-3: Simulated equifrequency contours for a 2D rod-based PhC with a square lattice having lattice constant $a = 437.5$ nm, rod diameter $d = 250$ nm, and rod height $h = 700$ nm. Super-collimation is seen to occur at a wavelength close to $\lambda = 1550$ nm.

for small changes δn, is proportional to a change in the wave-vector δk by the group velocity v_g. A change in the wave-vector will result in a phase shift. The distance L in which a phase shift of π is obtained between the two arms is the metric for sensitivity. Analysis utilizing perturbation theory arrives at the following distances for rods (L_r) and holes (L_h),

$$L_r = 5.7 \left(\frac{n}{\delta n} \right) \times 10^{-5} \text{ cm} \tag{2.19}$$

$$L_h = 3.4 \left(\frac{n}{\delta n} \right) \times 10^{-4} \text{ cm} \tag{2.20}$$

where n is the refractive index and δn is an incremental change in refractive index.

As expected, the distance needed to obtain a π phase shift is shorter for the rod-based super-collimator, making it more sensitive by a factor of 6. For example, a fractional change in n of 1 in 1000 would result in a L_r that is less than 600 μm. Immediately, one realizes that such a Mach-Zehnder design can be used as the backbone for an integrated chemical sensor chip. More details about the sensor and other applications are discussed in Chapter 5. Most of the simulation and theoretical results presented were contributed by Andre Kurs, advised by Marin Soljačić, in the ab initio Physics Group.

Chapter 3

Fabrication Approach

The super-collimator that is designed is a 2D photonic crystal with a square lattice of rods. Figure 2-2 depicts the dimensions of the target device and is reproduced below as Figure 3-1. To pattern the rods, interference lithography with a HeCd ultraviolet (UV) laser is used. Interference lithography is a very useful method for defining 2D periodic patterns. The device is fabricated in the top Si layer, also called the Si device layer, of an SOI wafer purchased from Soitec.

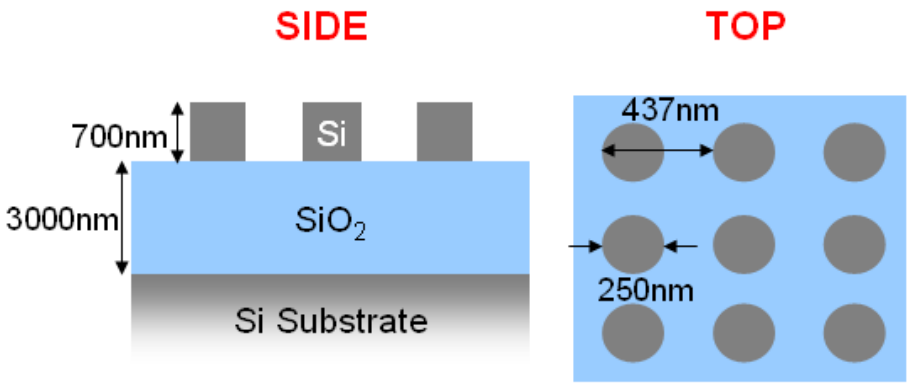

Figure 3-1: The 2D rod-based PhC that is designed to super-collimate at $\lambda = 1550$ nm.

After pattern definition, reactive ion etching (RIE) is used to transfer the pattern through the intermediary layers into the Si device layer. The RIE chemistries and other parameters are optimized to increase the uniformity and decrease the sidewall

roughness. Process optimization is important since a typical device (on the order of 1 cm^2 in size) consists of around 500 million rods. Two fabrication methods are presented below that are mainly distinguished by the chemistry with which the Si device layer is etched. Silicon can be dry-etched with two types of chemistries: fluorine-based or chlorine-based. The process that includes a fluorine-based RIE of silicon will be referred to as the Lift-off Process, and the process that includes a chlorine-based RIE of silicon will be referred to as the Main Process.

3.1 Interference Lithography

Interference lithography (IL) is a method of maskless lithography commonly used to pattern a large area with a grating or grid [3, 17]. IL involves the interference of two plane waves that are incident upon the sample. These two plane waves produce a standing wave pattern that is imaged into the photoresist, as shown in Figure 3-2.

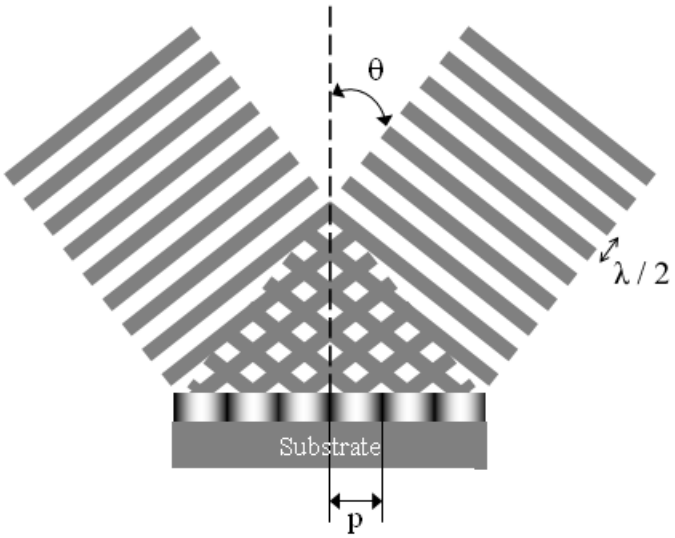

Figure 3-2: IL involves the interference of two plane waves to create a standing wave pattern that is imaged into the photoresist. Adapted from [3].

The standing wave intensity pattern has the form [18]

$$I = A_1 \sin^2 \frac{\pi}{p_1} x \tag{3.1}$$

and satisfies [17]

$$p_1 = \frac{\lambda}{2}\sin(\theta) \tag{3.2}$$

where I is the intensity of the light at the surface, λ is the wavelength of light, p_1 is the period of the standing wave intensity pattern, θ is the angle of incidence, and A_1 is a constant set by the exposure dose.

The period of a grating can be changed by adjusting the angle θ, while the linewidth is changed by adjusting the exposure dose. For the purposes of fabricating a 2D photonic crystal of rods with a square lattice (grid pattern), two orthogonal exposures are used. The intensities of the two exposures add, resulting in an intensity distribution of the form [18]:

$$I = A_1 \sin^2 \frac{\pi}{p_1}x + A_2 \sin^2 \frac{\pi}{p_2}y \tag{3.3}$$

A_1 and A_2 are constants set by the respective exposure doses, and p_1 and p_2 are the respective periods. The 2 periods can be changed by adjusting the angle θ for each exposure, and the size of the holes or rods along each direction can be set by adjusting the exposure dose for each exposure. For the purposes of fabricating a uniform 2D photonic crystal, $A_1 = A_2$ and $p_1 = p_2$. The resulting intensity distribution is plotted in Figure 3-3.

The IL system that is used for the fabrication of the super-collimators in the thesis is the Lloyd's Mirror depicted in Figure 3-4. The laser beam from the HeCd UV (λ = 325 nm) laser is sent through a spatial filter to eliminate high-frequency noise. The resulting Gaussian beam is incident upon the mirror and sample. The mirror is positioned 90° to the stage where the sample rests. By rotating the stage, the angle θ can be adjusted. Because the laser power is not changed, the exposure dose is set by the exposure time in practice. The Lloyd's Mirror is analyzed in detail in [3, 17, 19].

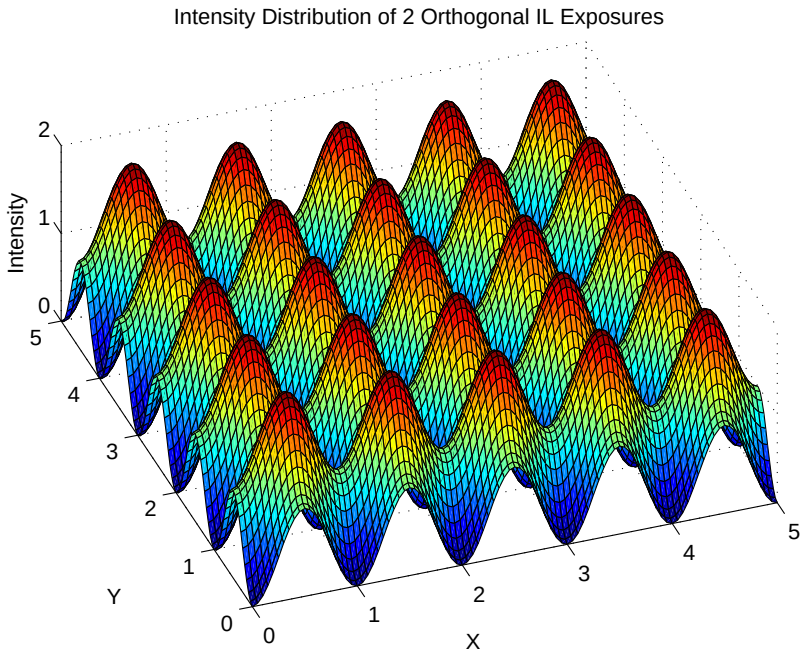

Figure 3-3: The graph of Equation 3.3 with $A_1 = A_2 = 1$ and $p_1 = p_2 = 1$.

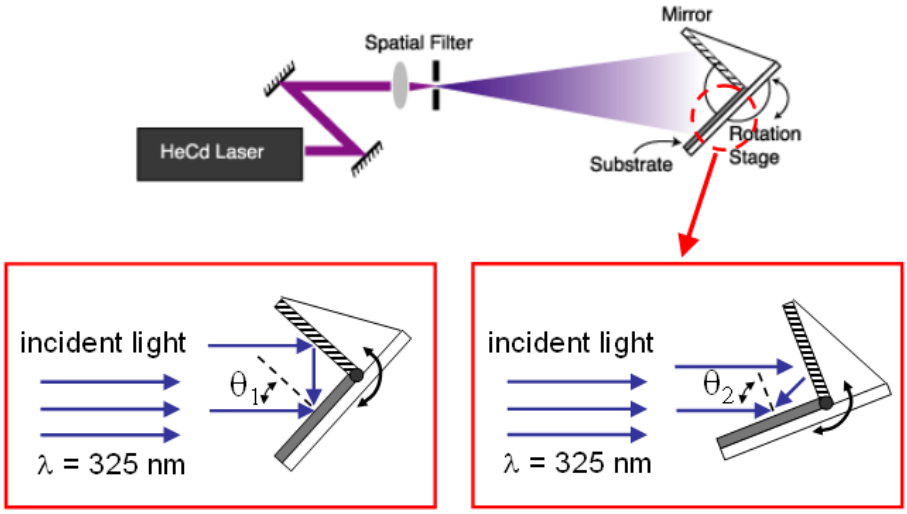

Figure 3-4: The Lloyd's Mirror IL set-up. The angle θ is set by turning the entire stage. Images adapted from [3, 17].

3.1.1 Rod and Hole Pattern Definition

At first glance, the best way is to pattern holes and rods may not be obvious. To maximize image contrast, it turns out, holes should be patterned with negative photoresist (PR) and rods with positive PR [18]. The image contrast K is defined as

$$K = \frac{I_{max} - I_{min}}{I_{max} + I_{min}} \tag{3.4}$$

where I_{max} is the maximum intensity and I_{min} is the minimum intensity.

K ranges from 0 to 1, and higher K is desired. In Figure 3-3, the local minimums have intensities of zero, the local maximums have intensities of what will be called I_o, and the saddle points have intensities of $I_o/2$. To define rods in negative resist, the rods would need to occur at the local maximums. In the worst case scenario, $I_{max} = I_o$, $I_{min} = I_o/2$ (saddle points), and $K = 1/3$. On the other hand, to define rods with positive PR, the holes would need to occur at the local minimums. In the worst case, $I_{max} = I_o/2$ (saddle points), $I_{min} = 0$, and $K = 1$. Thus, from the point of view of image contrast, positive PR should be used for rods. Along the same lines, negative PR should be used for holes to maximize the image contrast K. The argument for holes is similar to that for rods.

Image contrast is not the only factor that should be taken into account, however. The shape of the rods is another important element, because the shape changes as exposure dose is adjusted. Consider the latent image in the PR during an exposure. A high-contrast positive resist will be used for this example, so the resist sidewalls will be near-vertical. The latent image is then a cross-section at the PR's clearing dose of the intensity distribution in Figure 3-3. For small doses, a cross-section near the maximums of the intensity distribution is sampled, and holes are defined. The resulting resist profile is depicted in Figure 3-5, left. For large doses, a cross-section near the minimums of the intensity distribution is sampled, so rods are defined. The resulting resist profile is depicted in Figure 3-5, right. Calculations and the figures show that the holes and rods are quite circular in cross-section. For negative resist, the geometry is simply inverted.

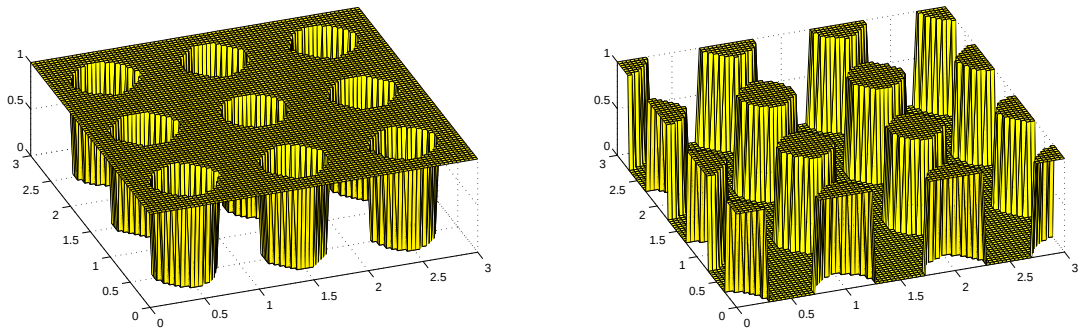

Figure 3-5: Far below (left) and above (right) the Crossover Dose, the photoresist holes and rods have circular cross-sections. A positive resist is assumed here, and lengths are in arbitrary units.

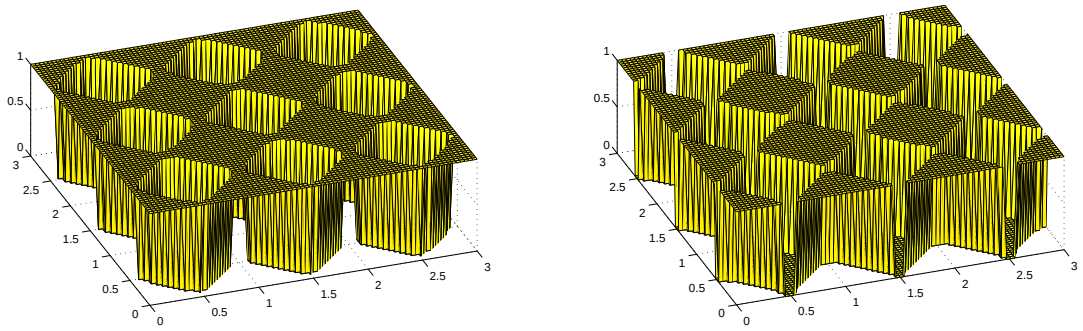

Figure 3-6: Near the Crossover Dose the photoresist holes (left) and rods (right) have square-shaped cross-sections. A positive resist is assumed here, and lengths are in arbitrary units.

The dose is set by the exposure time in practice, because the laser intensity is constant. Near the beginning of an exposure, the latent image consists of holes. As the exposure time is increased, the sampled cross-section moves lower in position until eventually rods are defined. Recall that the clearing dose of the PR does not change, but rather, the intensity distribution grows as the exposure dose is increased. The dose at which holes turns into rods will be defined as the Crossover Dose D_{co}. At D_{co}, the middle of the intensity distribution is sampled, at the height of the saddle points. Calculations show that when the dose is near D_{co}, the holes and rods become more square-shaped. The PR profiles are shown in Figure 3-6.

Unfortunately, the exposures for the super-collimating devices are performed at a dose in the vicinity of D_{co}. The diameter of the rods in the super-collimator design

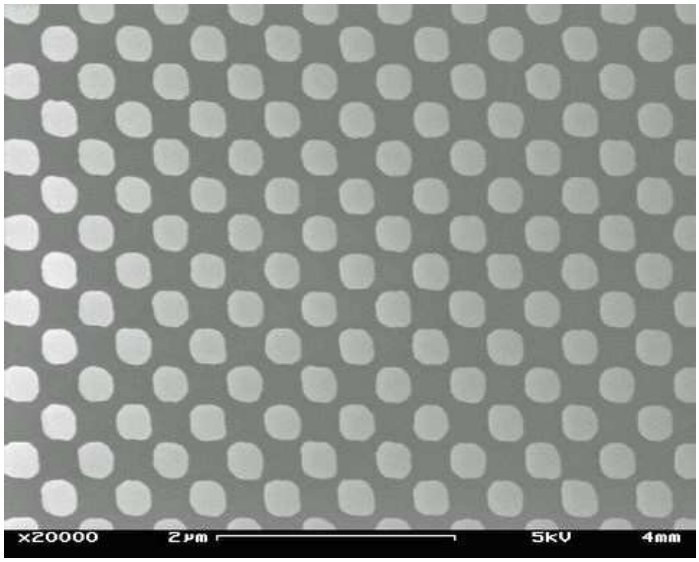

Figure 3-7: A square-like shape is visible in the SiO_2 etchmask as imaged from the top of a finished Main Process device. The exposure time was 125 s at a laser power of 0.48 mW.

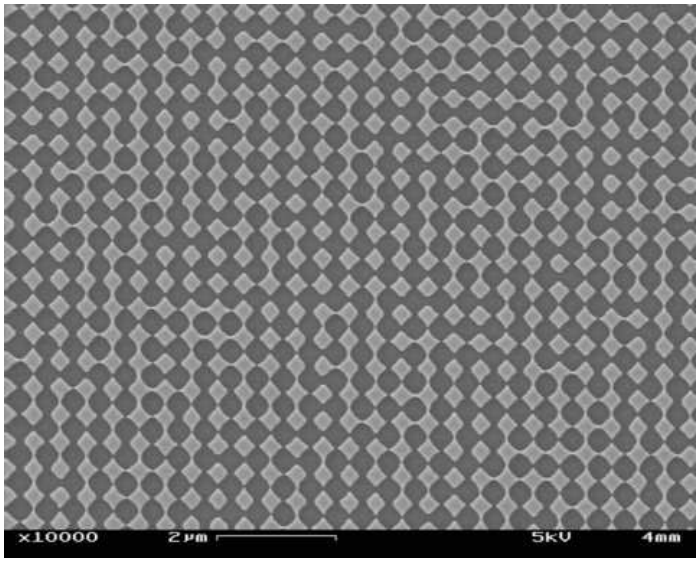

Figure 3-8: Near the edge of a large sample, the pattern in SiO_2 on SOI wafer of a Main Process sample consisted of a combination of rods and holes. Exposure was for 125 s at a laser power of 0.48 mW.

was close enough to the period that a rounded square-like rod shape was observed, as shown in Figure 3-7. Even though the design was for circular rods, the fabricated device with rounded square-shaped rods still exhibited super-collimation.

Near the Crossover Dose, the tolerances for pattern definition are very narrow. A slight variation in any parameter can cause the rods to touch and form holes instead, or vice versa. Some edges of a sample (of size approximately $(1.3\text{ cm})^2$) are unusable since small variations cause the pattern to be a mixture of rods and holes. Figure 3-8 is a scanning electron microscope (SEM) image of the SiO_2 etchmask pattern near a corner of a sample, before etching of the Si layer. Away from these edges, the pattern is usually as desired. However, the boundary between the two regions is unclear. For any particular section of a sample, little information was known about whether it was usable. Furthermore, the samples could not be imaged with the SEM before measurement, because prior to imaging in a SEM, devices need to be sputter-coated with Au/Pd to prevent charging caused by the electron beam. The metal coating would alter the optical properties of the super-collimator. Each sample was thus cleaved into many smaller pieces, such that each device piece was small enough to ensure that some of them were entirely patterned as desired.

3.1.2 Sample Preparation

The fabrication processes that are used are planar processes, which means that the steps involve the addition of material or the subtraction of material in a planar fashion. Most semiconductor fabrication techniques are planar processes. Before any lithography or etch steps, different layers of material need to be applied onto the SOI wafer, as schematically shown in Figure 3-9.

The most important element is the photoresist, which is applied via spin-coating. The spin-coating parameters are included in Table A.2 in Appendix A. PS4 (manufactured by Okha America) is a chemically-amplified negative resist. PFI-88 (manufactured by Brewer Science) is a positive resist based on phenol-formaldehyde (novolak) resin with diazonaphthoquinone (DNQ) photosensitizers.

To minimize back-reflections from the substrate into the PR during exposure,

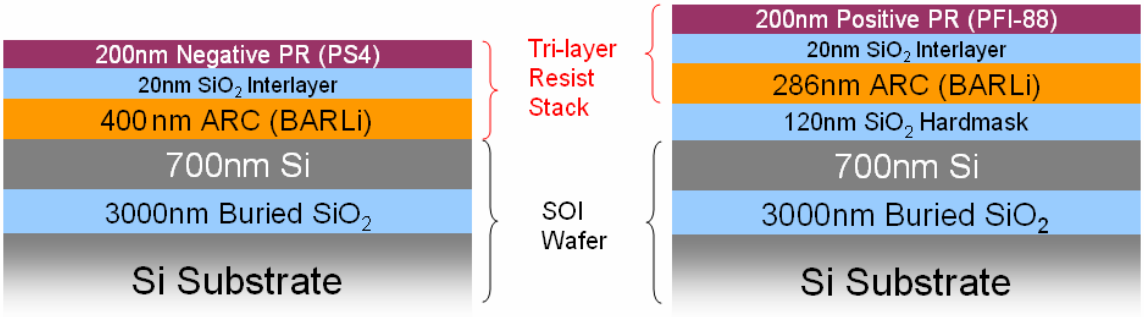

Figure 3-9: Sample preparation diagrams for the Lift-off Process (left) and the Main Process (right). Dimensions are not to scale. This is the state of the samples right before IL exposure.

an anti-reflective coating (ARC) was used: BARLi (manufactured by AZ Electronic Materials), a polymer that is applied below the PR layer via spin-coating. However, the RIE chemistry used to etch the ARC also etches the PR. Therefore, to improve the RIE etch selectivity for pattern transfer from the PR to ARC, an interlayer of SiO_2 is deposited onto the ARC with electron-beam evaporation prior to application of the PR. The CF_4-based reactive ion etch that is used to etch SiO_2 does not chemically etch the PR, and the RIE with O_2 used to etch the ARC does not chemically etch the oxide. The use of PR, SiO_2, and ARC is known as the tri-layer resist process, and the PR-oxide-ARC layers are known collectively as the tri-layer resist stack.

The ARC thickness is designed to minimize back-reflections from the substrate into the PR, i.e. at the interface between the PR and the SiO_2 interlayer. A simulation similar to the one used in [17] is performed to calculate the optimal ARC thickness. For the Lift-off Process, an ARC thickness of 400 nm is chosen. Although the reflectivity minimum at an ARC thickness of 400 nm is not the absolute minimum, as depicted in Figure 3-10, left, a thicker ARC layer helped to facilitate the lift-off step. From the simulation results in Figure 3-10, right, an ARC thickness of 286 nm is chosen for the Main Process. Table A.1 in Appendix A lists the refractive indices used in the simulation.

Notice that a hardmask layer is present in the Main Process but not in the Lift-off Process. In the Lift-off Process, the chromium hardmask is deposited later in the pro-

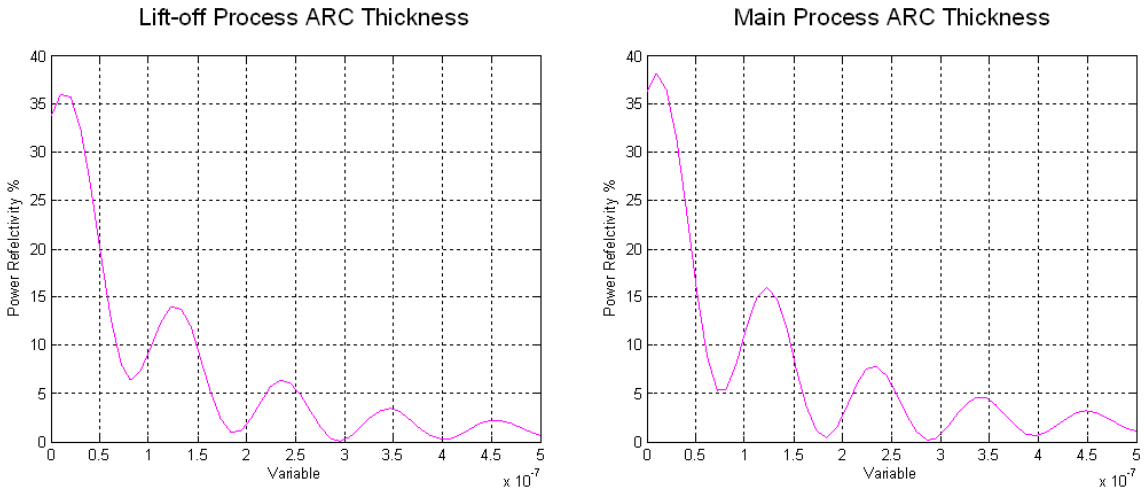

Figure 3-10: Left: for the Lift-off Process, the simulation indicates that the back-reflection into the PR will be minimized if the ARC layer has a thickness of 296 nm, but the local minimum of a thickness of 400 nm was chosen to facilitate the lift-off step. Right: for the Main Process, the simulation indicates that the back-reflection into the PR will be minimized if the ARC layer has a thickness of 286 nm.

cess during a lift-off step. For the Main Process, the hardmask layer is high-frequency SiO_2 deposited via Plasma-Enhanced Chemical Vapor Deposition (PECVD).

An adhesion promoter, hexamethyldisilazane (HMDS), is applied to the 20-nm SiO_2 interlayer, prior to spin-coating with PR, to avoid adhesion problems between the resist and oxide. HMDS is applied to the sample for 60 s, after which it is spun off at 1 krpm, leaving only a monolayer of HMDS on the oxide interlayer. One should wait at least 10 minutes before spinning PR after applying HMDS because the HMDS vapor can contaminate the PR.

Two fabrication methods are presented below: the Lift-off Process, followed by the Main Process. The Main Process is so named because the fabricated devices have been successfully characterized to exhibit super-collimation. The Lift-off Process is so named because the process contains a characteristic lift-off step. The devices fabricated with the Lift-off Process have not shown super-collimation as will be discussed shortly.

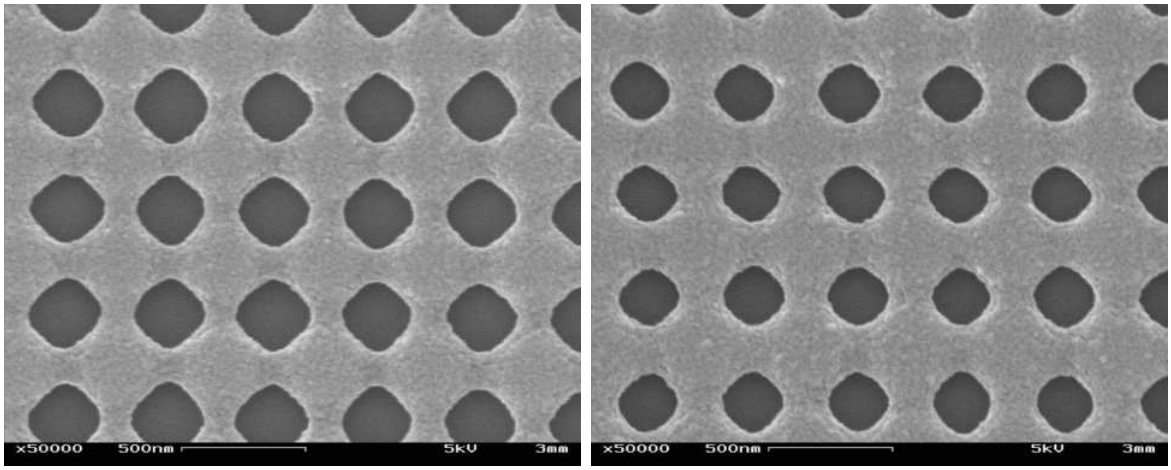

Figure 3-11: Developed PS4 photoresist on the SiO_2 interlayer: examples of monitor samples used to determine the correct exposure time for the pattern. The sample on the left was exposed for 15 s (in each orthogonal direction), and the sample on the right was exposed for 20 s (in each orthogonal direction).

3.2 Lift-off Process Fabrication

The Lift-off process flow is given in Figure 3-12.

3.2.1 Interference Lithography

Two orthogonal IL exposures are needed to form a grid pattern. A set of monitor exposures are performed prior to the exposures of the actual device samples. The monitor exposures are used to determine the exposure time, i.e. dose, of the desired pattern. Examples of monitor exposures are shown in Figure 3-11. Subsequent to exposure, each sample is developed in CD-26, 2.4% tetramethylammonium hydroxide and water solution (manufactured by Rohm & Haas), for 60 s, and then rinsed with deionized (DI) water.

For the Lift-off Process, holes are desired in photoresist, rather than rods. A negative photoresist, PS4, is used, which means an increased dose would define smaller holes. The size of the holes also need to be slightly larger than the target diameter of the rods because the lift-off process is not a perfect image reversal process. An SEM micrograph of the holes structure for a 17-second exposure at a laser power of 0.48 mW is shown in Figure 3-13.

Lift-off Process Flow

1. Bare silicon-on-insulator (SOI) wafer.

2. Spin coat with anti-reflective coating (ARC) (400nm thick).

3. Deposit SiO_2 interlayer using electron-beam evaporation (20nm thick).

4. Spin coat with negative photoresist (200nm thick)

5. Interference lithography with the Lloyd's Mirror (λ = 325nm).

6. Develop in CD-26 for 60s to obtain holes in photoresist.

7. Etch SiO_2 using reactive ion etching (RIE) with CF_4.

8. Etch ARC using RIE with He/O_2.

9. Deposit chromium using electron-beam evaporation (150nm).

10. Remove ARC in ARC-stripper (EKC-265) at 65ºC for 15min.

11. Etch Si using RIE with CF_4/O_2.

12. Remove Cr in chromium etchant (CR7) for 25min.

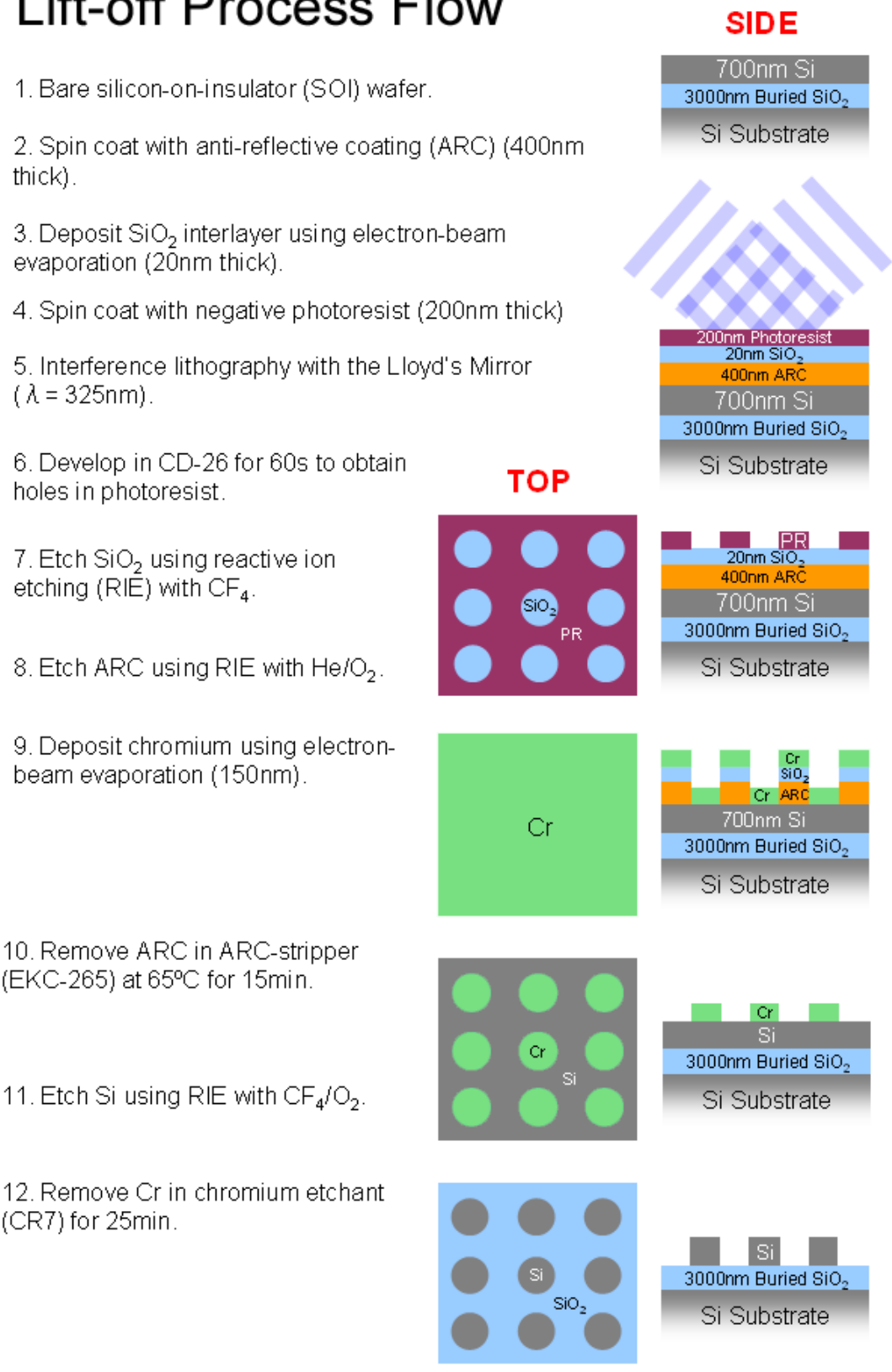

Figure 3-12: Lift-off Process Flow (dimensions not to scale).

3.2.2 Reactive Ion Etching

In order to transfer the pattern from the photoresist through the intermediary layers to the silicon, reactive ion etching (RIE) is used. RIE is a method of dry-etching that is capable of high anisotropy through the use of a combination of chemical plasma etching and ion bombardment. All of the RIE steps, with the exception of the RIE procedure using Cl_2 described in Section 3.3.3, were performed in a Plasma-Therm 790 RIE system.

A reactive ion etcher consists of a chamber with 2 parallel electrodes. The sample is placed on one electrode. The other electrode is grounded. Etch gases are introduced into the chamber, and a radio frequency (RF) voltage is capacitively coupled to the non-grounded electrode, ionizing the gas molecules and creating a plasma. The plasma's radicals, which are often neutral, and ions chemically etch the sample. Chemical etching occurs when a volatile species is formed from the reaction of a reactive species in the plasma with the material that is to be etched. For example, when Si is etched with a CF_4 plasma, SiF_4 is formed as a gaseous product, which desorbs from the surface of the sample. The RF fields in the chamber change direction with each cycle of the RF signal, causing the ions and electrons to experience a force towards one electrode and then the other. The electrons have very small masses and are accelerated into the two electrodes, while the ions are relatively uneffected. The non-grounded electrode builds a negative charge due to the absorbed electrons, and an equilibrium DC bias voltage is created between the positive ions in the plasma and the negative electrode. The DC bias causes the positive ions to accelerate toward the sample, resulting in ion bombardment. Reactive ion etching is due to the combination of chemical etching by the reactive species in the plasma and bombardment by the ions, which contributes to sputter etching as well as enhancing the chemical etching. An in-depth treatment of RIE can be found in reference [20].

Materials that are not etched chemically can still be etched by ion bombardment, or sputter etching. Sputter etching has etch rates that are normally much slower than the etch rates due to the combination of chemical etching and ion bombardment. A

well-designed RIE step only sputter etches the etchmask without chemically etching it. Sputter etch rates for masking materials are not interesting from a process point of view, however, because the mask layer is usually much thicker than what is needed.

There are several RIE parameters one can adjust to optimize a particular etch. The parameters are as follows: (1) gas flow, (2) RF power or DC bias voltage, (3) chamber pressure, and (4) etch time. Gas flow generally does not affect the properties of the etch, as long as the flow is large enough to ensure that the reactive agents are replenished faster than they are depleted through the chemical reactions, and that the pumping system maintains the desired chamber pressure. The chamber pressure indicates the number of atoms that will be available for etching. However, increasing the pressure also increases the particle collision rate, which decreases the anisotropy. The RF power ionizes the gas molecules into reactive ions and radicals. Increasing the power increases the number of reactive species available for chemical etching. In a conventional parallel-plate RIE tool, the RF power and the DC bias can not be set independently, as increasing the power increases the DC bias as well. The trade-off in DC bias voltage is as follows: a lower DC bias voltage is required to reduce the sputter-etching of the mask, while a larger DC bias is desired to increase the anisotropy. During an etch, one can control the RF power or the DC voltage, but not both. In a more advanced system such as an inductively coupled plasma (ICP) RIE system, the bias voltage and RF power are more decoupled. The pressure also affects the two parameters, but is controlled independently.

After development in CD-26, the pattern in PR is transferred into the SiO_2 interlayer using a CF_4-based RIE step. Fluorine-based RIE chemistries such as CF_4, SF_6, or CHF_3 chemically etch Si and Si-containing compounds, such as SiO_2. However, fluorine-based etches do not chemically etch organic substances like PR and ARC. A He/O_2 RIE step is used to etch the ARC. O_2 will chemically etch organics, but not Si-containing compounds. Helium is inert, and is added to decrease the partial pressure of O_2, thus slowing down the etch rate and making the etch more controllable. Because the He/O_2 RIE chemistry etches both ARC and PR, the PR is removed during the ARC etch. The resulting structure consists of holes in SiO_2 and ARC, as

shown in Figure 3-13. Table A.3 in Appendix A lists the RIE parameters that were used.

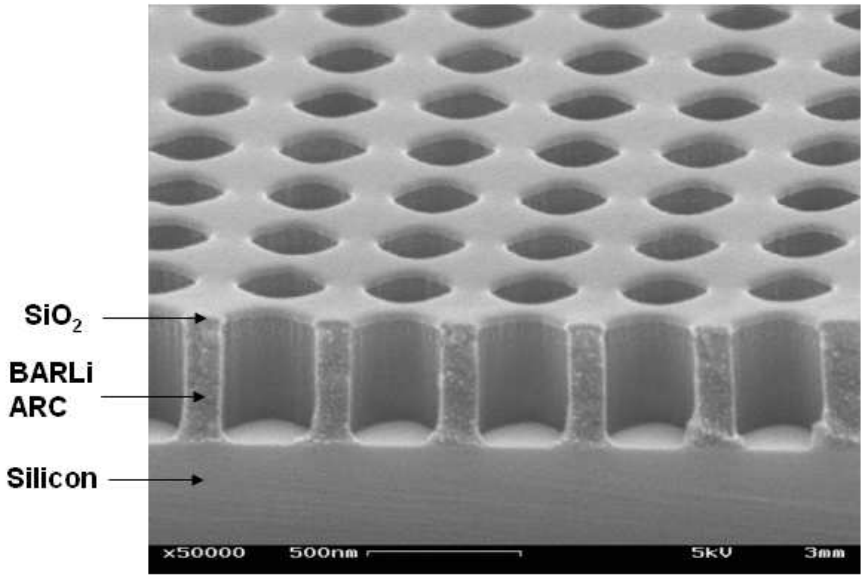

Figure 3-13: SiO_2/ARC holes on Si, prior to lift-off.

3.2.3 Lift-off

Lift-off is an image-reversal process that is often considered useful only in research. It is not often used in industry, despite its many useful applications. Lift-off is used in this process as a method for chromium pattern definition, the result of which is used as the hardmask for the RIE step with CF_4 to etch Si. Chromium can be patterned by etching as well, but lift-off was seen as a better-controlled method of pattern definition. Experiments of wet-etching chromium using a chromium etchant solution consisting of perchloric acid and ceric ammonium nitrate (manufactured by Transene) resulted in deformed structures due to non-uniform etch rates.

The lift-off process consists of two steps. First, 150 nm of Cr is deposited onto the sample in Figure 3-13 via electron-beam evaporation. Next, the ARC is removed in EKC-265 (manufactured by DuPont Electronics) at 65°C for 15 minutes, and rinsed with deionized (DI) water. This "lifts off" the Cr that was deposited onto

the SiO_2/ARC, and leaves the Cr that was deposited in the holes. The EKC-265 often left some residue on the surface of the Si substrate, but the residue did not seem to pose a problem for the subsequent RIE step. A monitor sample after lift-off is shown in Figure 3-14.

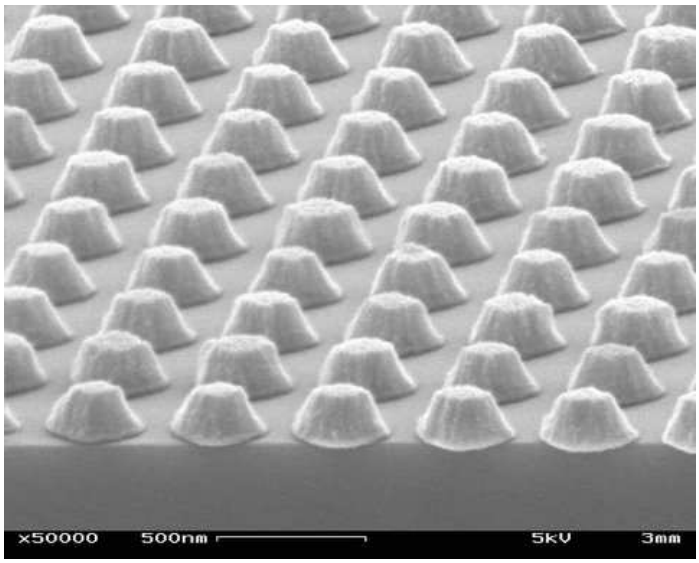

Figure 3-14: Cr rods on SOI wafer. The Cr rods shown here, which look more like mounds, are 120 nm high, instead of 150 nm used for the finished device.

3.2.4 CF_4/O_2 Si-RIE

The final step is to etch the silicon using a CF_4-based RIE step. The addition of O_2 to the RIE recipe has been shown to increase the etch-rate [21]. Thus, a combination of CF_4 and O_2 was used to etch the Si via RIE, at a CF_4-to-O_2 ratio of 13.5 to 1.5. The RIE parameters[1] are listed in Table A.3 in Appendix A. Following the RIE of Si, the Cr etchmask was removed in chromium etchant solution consisting of perchloric acid and ceric ammonium nitrate (manufactured by Transene) for 25 minutes. The finished device is shown in Figure 3-15.

The device has not been successfully measured, because the device was fabricated

[1]The RIE of Si with CF_4/O_2 was not performed as one continuous etch, but in intervals of 5:00, with 2:00 breaks to allow the sample to cool down. Ion bombardment heats the sample during an etch, and the change in temperature can alter the etch rate.

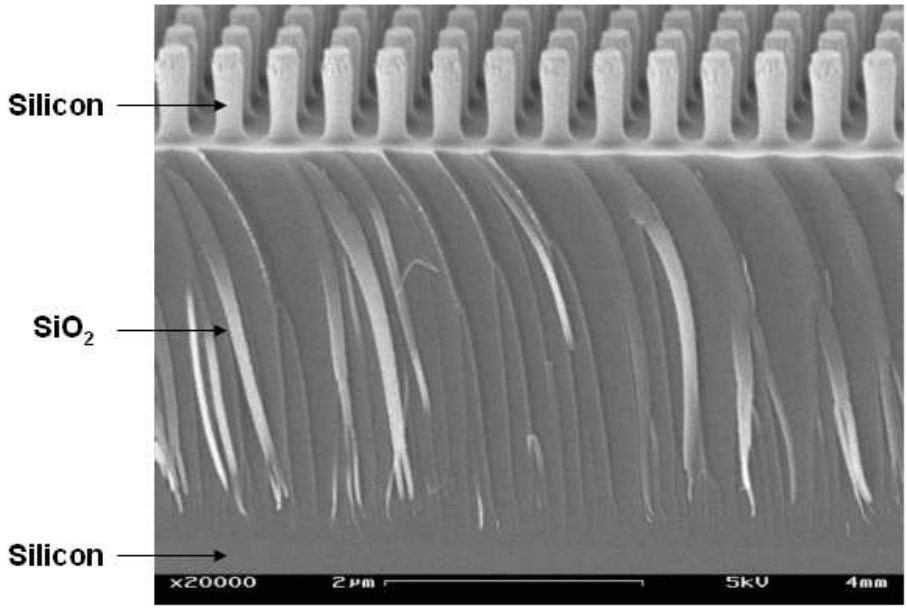

Figure 3-15: The finished 2D rod-based PhC super-collimator fabricated with the Lift-off Process. In the SEM micrograph, the 3 μm of SiO_2 is clearly visible, due to the distinct manner that SiO_2 often cleaves.

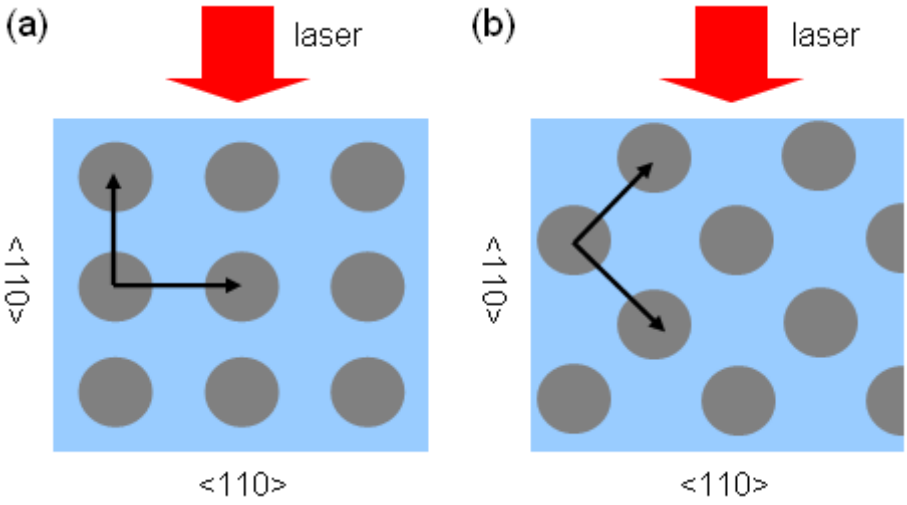

Figure 3-16: The laser beam is coupled into the super-collimator at normal incidence. (a) The orientation of the pattern on the samples fabricated with the Lift-off Process did not allow light to be coupled into the super-collimator in the correct direction. (b) The orientation of the pattern for the Main Process samples were rotated 45° and allowed light to be coupled into the super-collimator in the correct (Γ-M) direction.

so that the square lattice was aligned with the wafer's cleave facets. The orientation is shown in Figure 3-16 (a). The SOI wafer has a crystal orientation of $\langle 100 \rangle$, and the cleavage planes are $\langle 110 \rangle$ planes. Cleaving 45° to the $\langle 110 \rangle$ planes along a $\langle 100 \rangle$ plane was found to be very difficult with the available tools. Recall that super-collimation occurs at 45° to the square lattice vectors, or along the Γ-M direction, meaning the samples needed to be patterned 45° to the $\langle 110 \rangle$ cleavage plane, as shown in Figure 3-16 (b). This was how the samples fabricated with the Main Process were oriented.

Because the RIE step with CF_4/O_2 etches SiO_2 as well as Si, the etch time must be controlled so that the 3 μm of buried oxide is not significantly etched. With fluctuations in power and voltage common to the RIE tool, preventing the SiO_2 from being etched was not an easy task. Devices were successfully fabricated (like the one shown in Figure 3-15), but with questionable reproducibility. A better approach would be to use an RIE chemistry that is selective to Si over SiO_2. The Cl_2-based RIE procedure used in the Main Process exhibits this selectivity, as discussed in the next section.

3.3 Main Process Fabrication

The Main process flow is shown in Figure 3-17.

3.3.1 Interference Lithography

Similar to the Lift-off Process, a set of monitor exposures are performed before the exposures for the actual device samples. The monitor exposures are used to determine the exposure time, i.e. dose, of the desired pattern. For the Main Process, rods, rather than holes, are desired in photoresist. Positive photoresist is used, so an increased dose would create smaller rods. The final exposure for the device was 125 s, at a laser power of 0.48 mW. The samples were developed in CD-26 for 60s. The rod pattern is shown in Figure 3-18.

Main Process Flow

1. Bare silicon-on-insulator (SOI) wafer.

2. Deposit SiO_2 using plasma-enhanced chemical vapor deposition (PECVD) (120nm thick).

3. Spin coat with anti-reflective coating (ARC) (286nm thick).

4. Deposit SiO_2 interlayer using electron-beam evaporation (20nm thick).

5. Spin coat with positive photoresist (200nm thick).

6. Interference lithography with the Lloyd's Mirror (λ = 325nm).

7. Develop in CD-26 for 60s to obtain rods in photoresist.

8. Etch SiO_2 interlayer using reactive ion etching (RIE) with CF_4.

9. Etch ARC using RIE with He/O_2.

10. Etch SiO_2 using RIE with CF_4.

11. Remove ARC using RIE with He/O_2.

12. Etch Si using RIE with Cl_2.

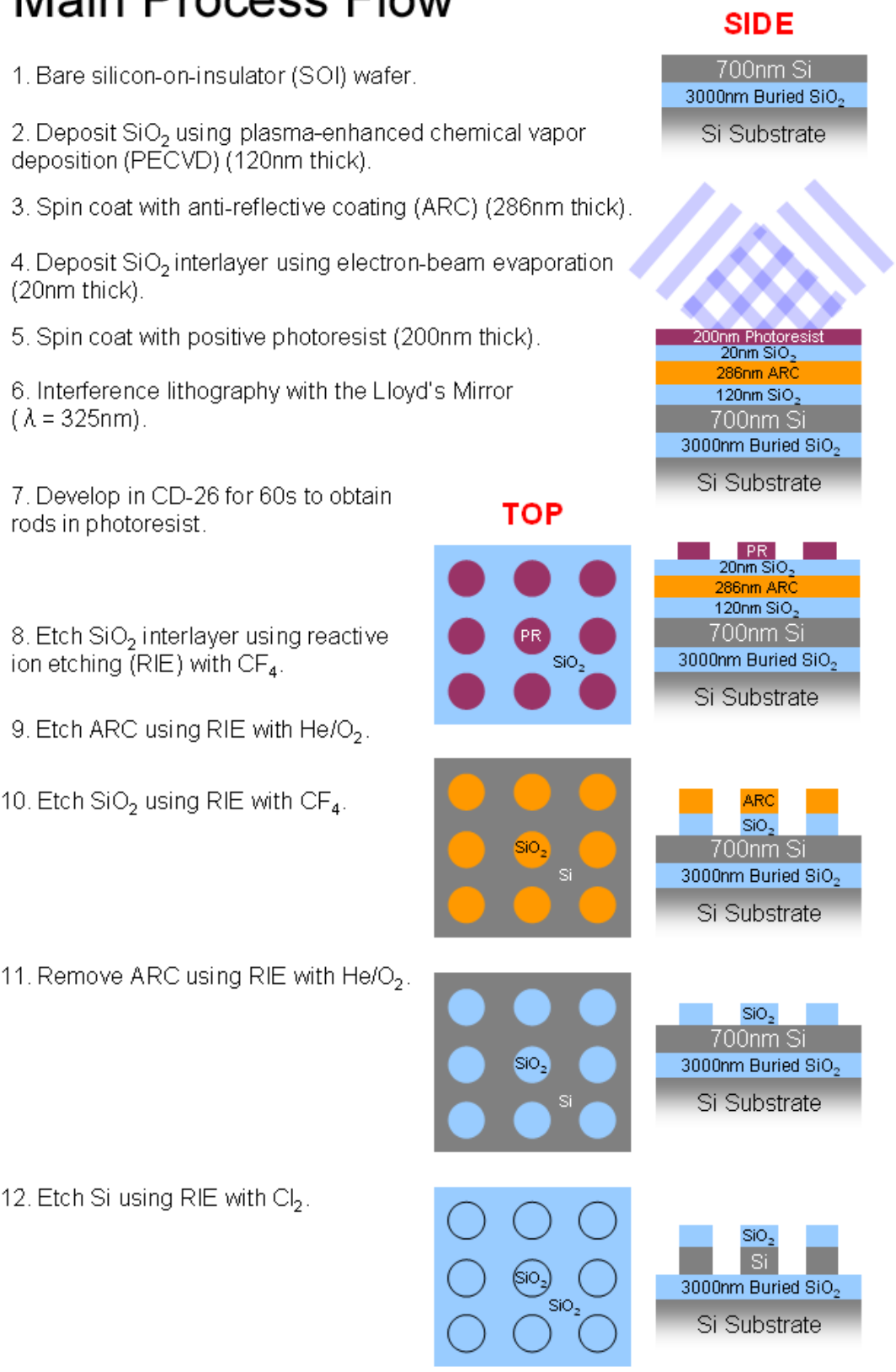

Figure 3-17: Main Process Flow (dimensions not to scale).

3.3.2 Reactive Ion Etching

After the PR is exposed and developed, the pattern is transferred into the SiO_2 using a RIE step with CF_4. Subsequently, RIE with He/O_2 is used to etch the ARC. A He/O_2 plasma will also etch photoresist, but not the oxide interlayer, so the resulting structure consists of rods in ARC with a layer of oxide on top. The photoresist is removed during the etching of the ARC layer.

Another CF_4-based RIE step is used to etch the 120nm-thick SiO_2 hardmask layer below the ARC. The RIE step also removes the 20 nm of SiO_2 above the ARC. RIE with CF_4 may etch into the Si layer; this slight over-etching does not present a problem. To etch the Si, RIE with Cl_2 is needed. In comparison, for the Lift-off Process, CF_4/O_2 was used to etch the Si layer. If RIE with CF_4/O_2 was used here, the ARC and SiO_2 etchmask would not withstand a reactive ion etch of 700 nm of Si. The ARC is sputtered relatively quickly, and the oxide is etched in a CF_4-based RIE step. In the Lift-off Process, chromium, which could withstand the etch, was used as the etchmask.

Before the Si layer is etched, the ARC is removed with another RIE step with He/O_2. Figure 3-18 shows the device after this process step. The ARC removal was thought to be superfluous at first, because the ARC added to the thickness of the SiO_2 hardmask for the subsequent RIE with Cl_2. However, the ARC was discovered to become hollow after a Cl_2-based reactive ion etch, as shown in Figure 3-19. This phenomenon has been observed before, and may be due to a "hardening" of the sidewalls of the ARC during the CF_4-based RIE of the SiO_2 hardmask. The subsequent RIE with Cl_2 then sputters through the "softer" inside of the ARC, leaving a hard shell behind. To avoid difficulties with the resulting ARC hard-shell, the ARC was removed prior to the reactive ion etch with Cl_2. The cause of the shell formation was not further investigated once the problem was bypassed. The complete set of RIE parameters can be found in Table A.4 in Appendix A.

Notice that there is no extra process step, such as lift-off, that is needed. Processing efficiency is one key advantage the Main Process has over the Lift-off Process.

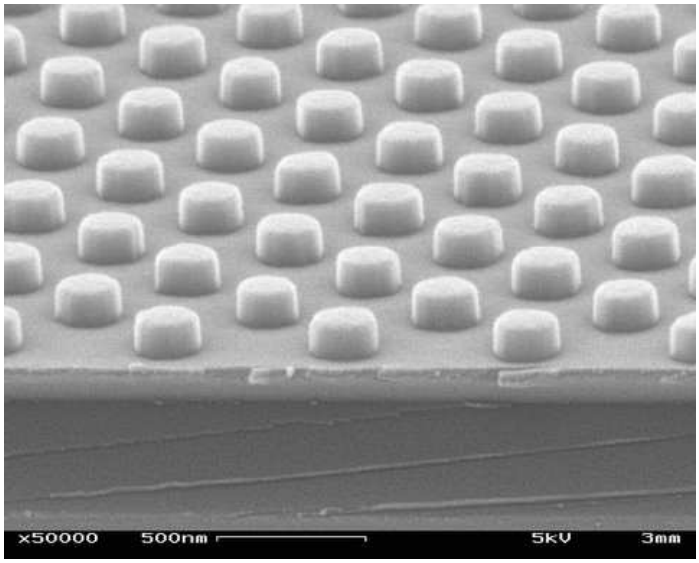

Figure 3-18: 120-nm-high SiO_2 rods on a SOI wafer. The sample was a monitor sample that was exposed for 135 s in each direction (not 125 s as for the finished device).

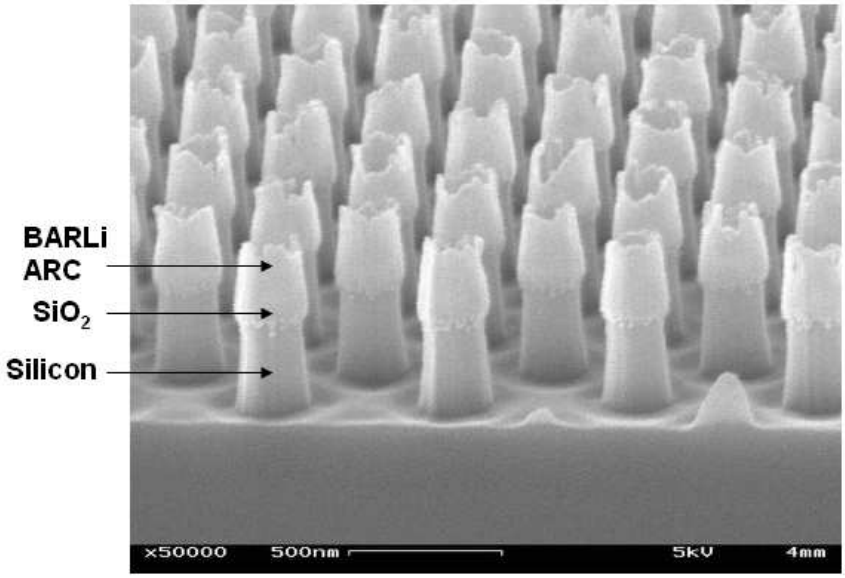

Figure 3-19: Hollowed ARC shells after a Cl_2 reactive ion etch. The boundary between the BARLi and SiO_2 is not clearly defined in the image.

3.3.3 Cl_2 Si-RIE

The final step in the Main Process is to etch into the silicon with RIE using Cl_2. The Cl_2-based RIE procedure was performed in a custom-built "Outerlab" RIE system in the Nanostructures Laboratory. Initial etches with the RIE tool resulted in micromasking, which causes what is called "black silicon" or "grass", as shown in Figure 3-20. The term "grass," although not technical, is seen to be very descriptive. The term "black silicon" arises because the surface of the grassy silicon looks black to the naked eye. Black silicon is desirable for some applications. For example, black silicon is purposely fabricated to create silicon surfaces that are more easily wetted [22]. However, for the application of interest here, black silicon is highly undesirable.

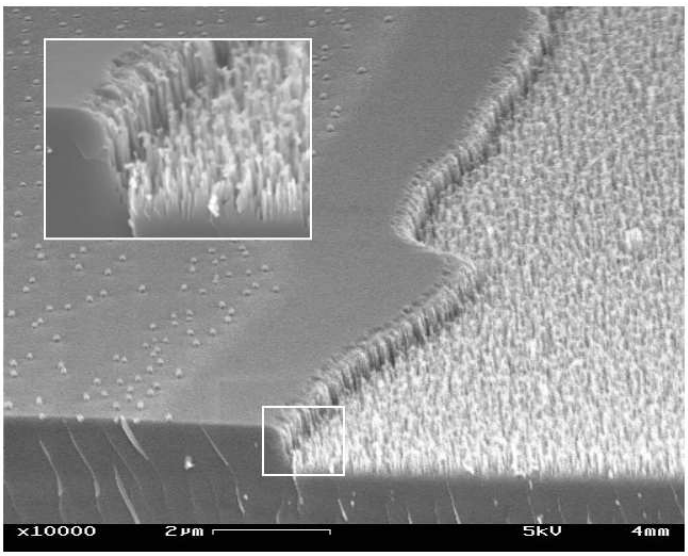

Figure 3-20: Contamination in the RIE chamber caused micromasking and produced many tiny rods, leading to "grass" or "black silicon," which is observed in the right part of the image. The left part is a layer of hydrogen silsesquioxane (HSQ) which masks the Si, and therefore grass is not observed. The inset magnifies the boundary between the grass and HSQ. Small particulates on the HSQ can be observed and are speculated to be due to contamination in the chamber. It is unclear why there seems to be an area along the edge where there are no particulates.

A cleaning/conditioning procedure that eliminated the grass was developed by Orit Shamir from the Integrated Photonic Devices and Materials Group. Her process consisted of (1) cleaning (RIE with CF_4/O_2), followed by (2) chamber coating (RIE

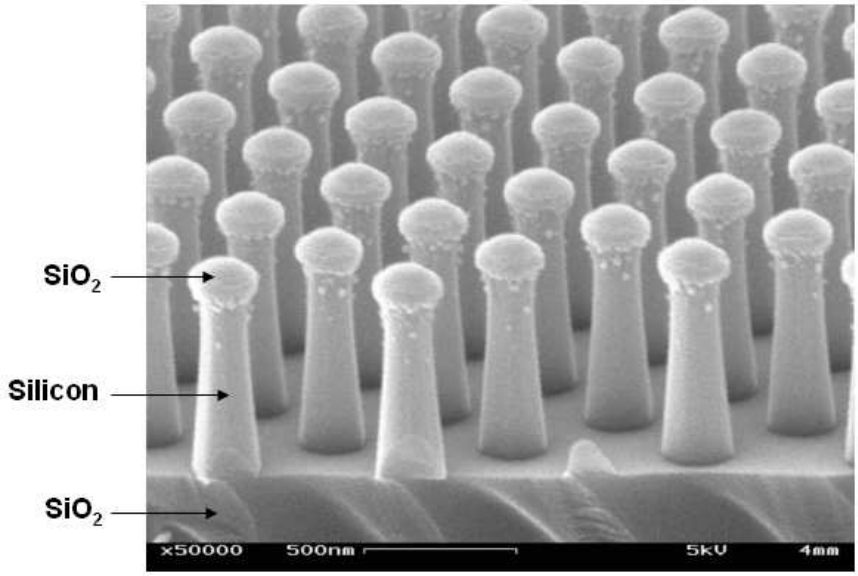

Figure 3-21: A successful Cl_2 reactive ion etch of Si. Tapering is very noticeable in this sample, which was a monitor sample that was exposed for 135 s in each direction (not 125 s as for the finished device).

with CHF_3/O_2), and ended with (3) chamber conditioning (RIE with Cl_2). When this cleaning/conditioning procedure was executed prior to a Cl_2-based RIE of Si, clean, grass-free etches were obtained. The chamber cleaning is believed to remove residue from the walls of the chamber. The chamber coating step then covers the chamber walls with a teflon-like coating that prevents microparticles from falling onto the sample. The final conditioning step prepares the chamber for the actual Cl_2 run. Figure 3-21 is an SEM image of a successful Si etch. The parameters for the three-step cleaning/conditioning procedure can be found in Table A.5 in Appendix A.

An RIE step using Cl_2 does not chemically etch SiO_2, whereas an RIE step using CF_4/O_2 does. In the case of the Cl_2-based RIE step, the buried oxide serves as an etch-stop layer for the Si etch. To reduce the variability, the sample is over-etched, since the etch rate slows down dramatically upon reaching the buried oxide layer. The final silicon etch is crucial and the existence of an etch stop layer is another advantages that the Main Process has over the Lift-off Process.

In Figure 3-21, the Cl_2-based reactive ion etch is seen to cause the Si rods to

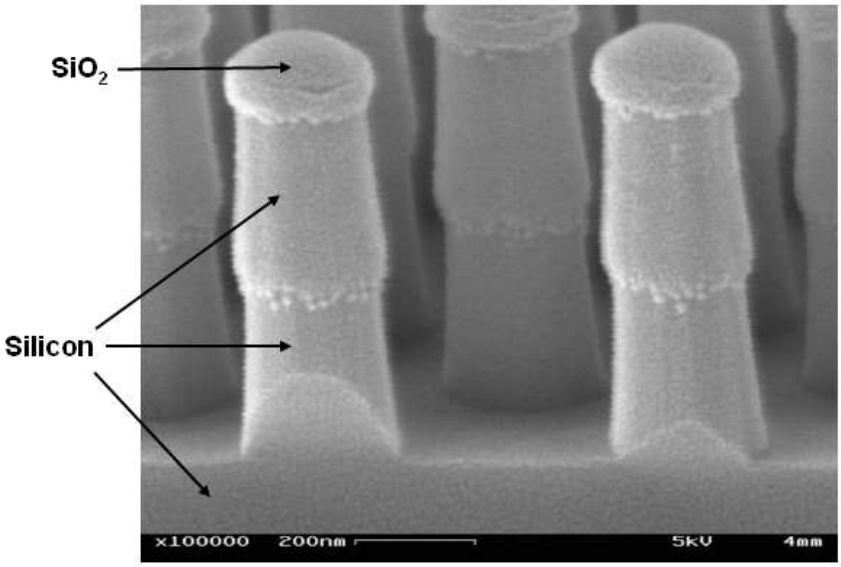

Figure 3-22: The result of an experiment to reduce the tapering. The sample was etched in Cl_2 for 5 minutes, removed from the RIE chamber for 1 hour, and then etched in Cl_2 for 5 more minutes.

taper, due to the isotropic etching of the Cl_2 plasma. In reactive ion etching, ion bombardment helps to produce a directional etch, but some lateral eching will still occur, and is reflected in rods that are wider at the bottom. A lower pressure and a higher voltage/power combination was used to increase the directionality of the etch, but tapering was still noticeable.

To remedy the tapering, the sidewalls of the rods were oxidized in the middle of an etch. The idea was to dramatically slow down the lateral etching by masking the sidewalls with native oxide. Experiments were performed in which samples were etched half-way, taken out of the RIE chamber (for at least 60 minutes) so that native SiO_2 was formed from the Si and ambient O_2, and then etched the rest of the way. The tapering was reduced, but the location where the first etch ended and the second began was rough and abrupt as shown in Figure 3-22. The roughness was less desirable than the tapering, and the sidewall passivation procedure with native oxide was not further pursued. Furthermore, simulations of the tapered rods showed that super-collimation was still possible (see Figure 3-23).

The final device is shown in Figure 3-24. The devices fabricated with the Main

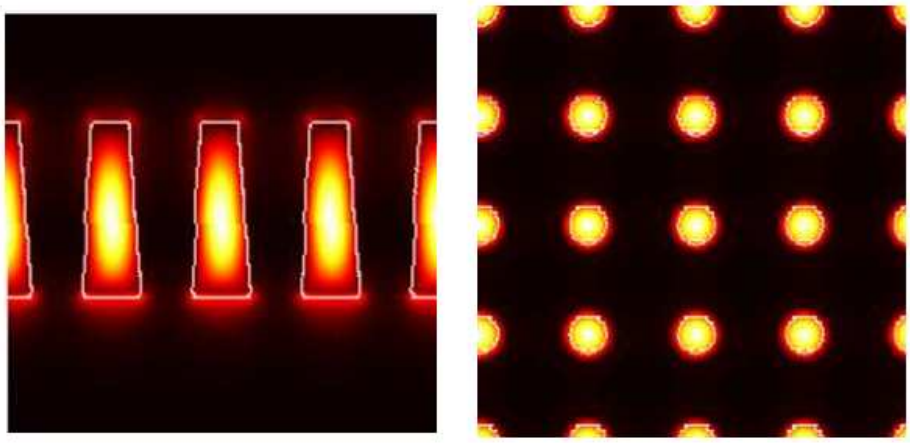

Figure 3-23: The intensity profile of a mode in the super-collimated region, as viewed from the side (left) and from the top (right). The shape of the tapered rods, shown by the white lines, are superimposed. The simulation shows that the modes are well-confined to the plane of the slab, allowing super-collimation to occur in a device with tapered rods.

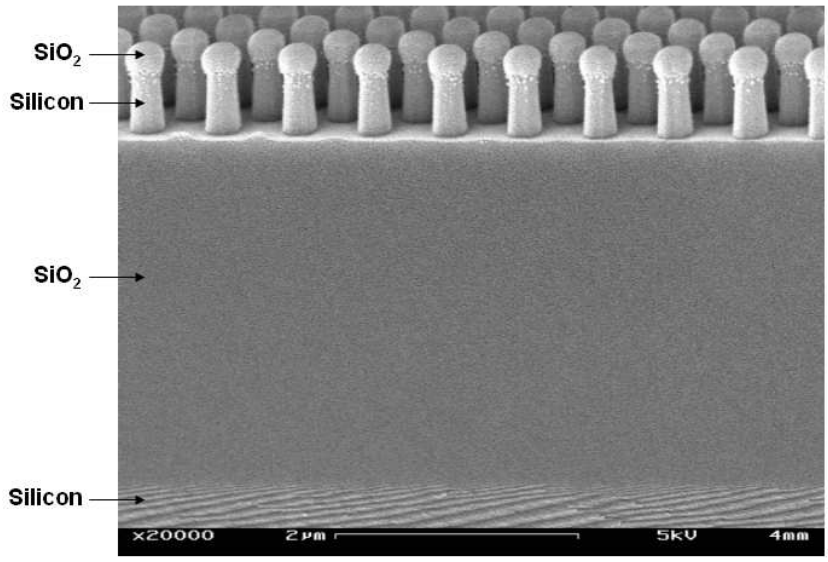

Figure 3-24: The finished 2D rod-based PhC super-collimator fabricated with the Main Process. In this SEM micrograph, the 3 μm of SiO_2 is clearly visible, due to the distinct manner that Si often cleaves.

Process have been successfully measured to exhibit super-collimation. SiO_2 is a low-index material at the operating wavelength of 1550 nm, so the oxide caps (left-over etchmask) on the Si rods were not removed.

3.4 Device Statistics

The properties of a photonic crystal arise from its periodicity. Therefore, the uniformity of the fabricated structures is an important property to characterize. Also important is an understanding of the process steps that introduce variations and of the methods to reduce the variations. As a motivation, consider the top-down SEM image that was taken with the Raith 150 Scanning Electron Beam Lithography tool shown in Figure 3-25, of a device that was fabricated with the Lift-off Process. The rods exhibit sidewall roughness and do not, at least qualitatively, appear to be uniform.

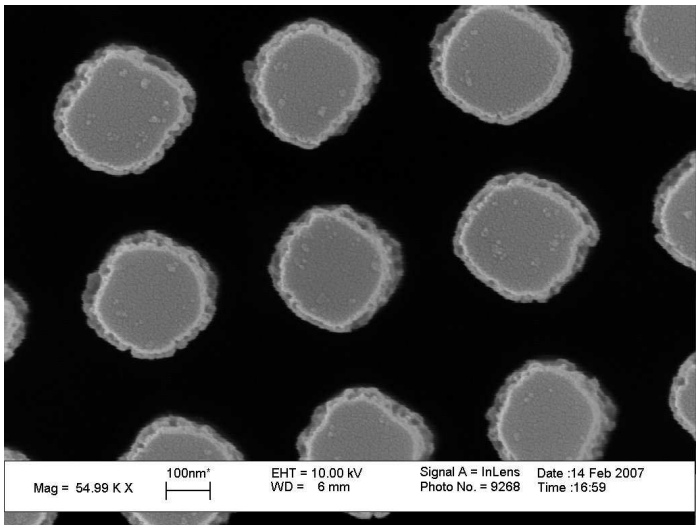

Figure 3-25: Top-down view of a Lift-off Process device taken with the Raith 150 Scanning Electron Beam Lithography tool. The Cr etchmask has been removed to reveal the flat tops of the Si rods. The variation in the shapes of the rods and sidewall roughness can be seen clearly.

The lift-off and subsequent RIE with CF_4/O_2 were hypothesized to introduce most of the variability. What was believed to be observed was that the lift-off process

created mounds of Cr, as seen in Figure 3-14, that had very non-vertical, rough sidewalls. When the Cr was used as an etchmask for the subsequent etch of Si, nonuniform Si rods were created.

Statistical methods were employed to test the hypothesis. A reasonable assumption was that for any given process step, the diameter of the features, whether they be rods or holes, was distributed normally with some mean and standard deviation. The variability could be due to nonuniform exposure, development, etching, or simply random "noise" from the fabrication. In order to estimate the variabilities, or standard deviations of the distributions, a pseudo-random sample set was obtained from top-view scanning electron micrographs. The sampling was "pseudo-random" because the location of the image on the device sample was randomly chosen to be characteristic of the entire device, but the rods that were analyzed were all from the same SEM image. The assumption is that this type of sampling is "random enough" to provide quantitative comparisons of the devices in various steps of the process.

The statistic that is often used to estimate population variance from sample variance is s_x^2, given by the following formula [23]:

$$s_x^2 = \frac{\Sigma(x - \bar{x})^2}{n - 1} \tag{3.5}$$

where n is the number of samples, $\bar{x}$ is the sample mean, and x are the sample values.

From s_x^2, the population variance, σ^2, can be estimated because the sampling distribution of s_x^2/σ^2 is well-known for each value of n. A rejection level of 5% was chosen, or equivalently, a range of possible σ^2 was found based on s_x^2, such that the probability that σ^2 was the true population variance was greater than 5%. Cutoff values for s_x^2/σ^2 with $n \approx 500$ of 0.878 and 1.13 were used [23].

Top-down SEM images of the following Lift-off Process samples were analyzed: (1) holes in SiO_2 and ARC (pre-lift-off), (2) Cr etch mask (post-lift-off), and (3) rods in Si (post- lift-off, RIE, and Cr removal). The histograms of the diameter of the sample sets are plotted in Figures 3-26 and 3-27, left. The population standard deviations, along with margins of error, are given in the first 3 rows of Table 3.1. The diameter

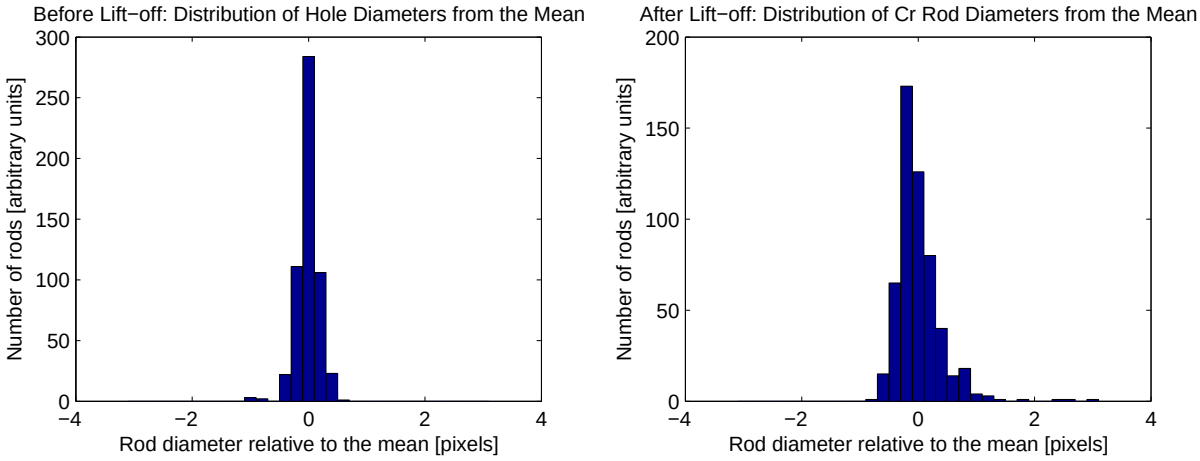

Figure 3-26: Histograms of diameters for a Lift-off Process sample before (left) and after (right) the lift-off process.

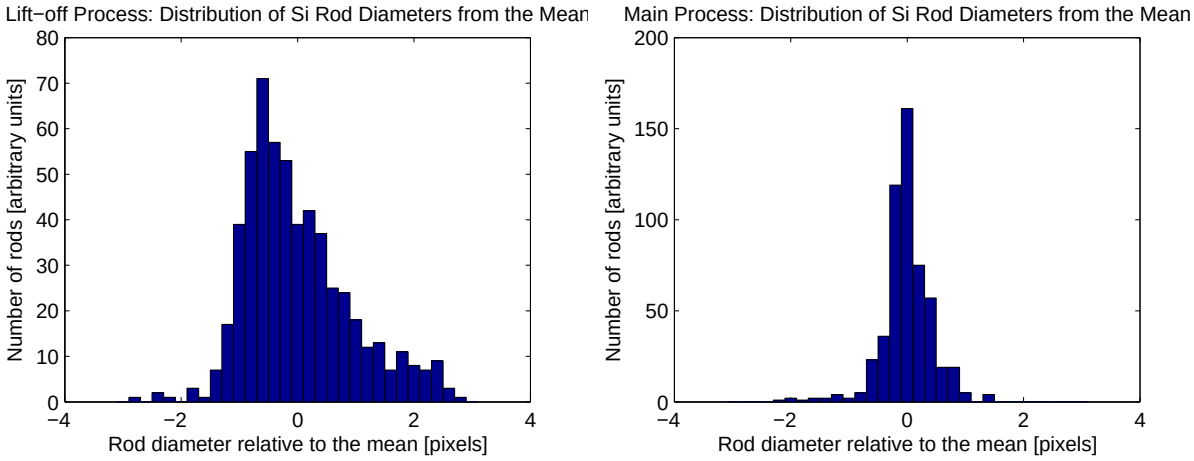

Figure 3-27: Histograms of diameters for a Lift-off Process super-collimator (left) and a Main Process super-collimator (right).

Table 3.1: Estimated population standard deviation of feature diameters in units of pixels. Note: the image used to determine σ of the SiO_2/ARC holes was of a sample with slightly smaller features (longer exposure time) than the sample of Cr rods and the finished Lift-off Process device, resulting in the discrepancy in $\bar{x}$. The diameter variability is not believed to be a strong function of diameter size, however.

Process Stage	**Population Standard Deviation σ**	**Sample Mean $\bar{x}$**	**Sample Size**
SiO_2/ARC Holes	0.189 ± 0.0127	11.2	552
Cr rods	0.380 ± 0.0256	15.3	544
Finished Lift-off	0.918 ± 0.0617	15.9	563
Finished Main	0.428 ± 0.0287	17.1	537

of the Si rods of the super-collimator was distributed with a population standard deviation of $\sigma = 0.918 \pm 0.0617$ pixels, compared to $\sigma = 0.380 \pm 0.0256$ before the etch, and 0.189 ± 0.0127 before lift-off. The RIE of Si using the lift-off Cr mask is seen to be the main source of variability. Nonuniformity in plasma etching at this microscopic level is often attributed to nonuniform mask patterns [24]. Because the mask pattern is periodic for a super-collimator, significant nonuniformity due to an RIE step is not expected, unless it is introduced by sub-microscopic nonuniformities in the etchmask. The Cr etchmask rods have slanted, rough sidewalls that do not contribute considerably to the variability from a top-down point of view, but after etching, the pattern transferred into the Si exhibits respectable variability.

On the other hand, the Main Process does not have a lift-off step, so the variability of the super-collimator should be reduced. A device fabricated with the Main Process was analyzed and the histogram of the sample set of diameters is shown in Figure 3-27, right. The rod diameter had a population standard deviation of $\sigma = 0.428 \pm 0.0287$. From the top, the SiO_2 caps were imaged, not the actual Si rods. However, the variability of the oxide caps are representative of the variability of the Si rods, because the oxide caps were imaged post-etch. Furthermore, significant nonuniformity due to an RIE step is not expected from the SiO_2 etchmask which had very vertical sidewalls with little roughness, as shown in Figure 3-18.

The super-collimator that was fabricated with the Main Process exhibits better rod uniformity than the super-collimator that was fabricated with the Lift-off Process. The sidewalls of the rods of the Main Process super-collimator are also smoother. These characteristics, along with having no lift-off step and an etch-stop layer for the Si etch using Cl_2, makes the Main Process the superior fabrication method.

To qualify the numerical results that were presented, the algorithm used to obtain the statistics will be briefly discussed. Top-view SEM images of the samples were used for statistical analysis. Digital SEM images are gray-scale TIFF files with 8-bits of gray-level. First, each pixel was quantized to 1 or 0 by comparison with a "threshold" value. The effective rod size changes depending on the "threshold" value chosen, leading to a source of error. The pixels of the SEM image are another source

of error. The number of pixels defining a rod, depending on the SEM image, can range from 80 to 400. When there are only 80 pixels in a rod, an error of 1 pixel results in an error of more than 1%. The most accurate "threshold" value can be found without difficulty to a precision of ± 10, or $\pm 4.0\%$, of the 8-bit range. Changing the "threshold" value by $\pm 4.0\%$ of the 8-bit range changed the resulting standard deviation of the diameter by a maximum of ± 0.0867 pixels for the "Finished Lift-off" image, and much less for the other images. Despite these sources of error, the confidence of the several comparisons made above are seen to remain high.

Once the image was quantized, the image was scanned for groups of 1's. The "rod" or "hole" pixels are quantized to 1, and the "surface" pixels to 0. If a pixel is found belonging to a rod or hole, a recursive function calculates the number of pixels defining the rod, or equivalently, the area A. Only adjacent (top, down, left, right) pixels are considered to be part of the same rod. Diagonal pixels are not considered adjacent. Outliers are eliminated. Most often, outliers are due to rods that are cut at the edges of an image.

The area A is then converted into a diameter d by approximating the rod as a perfect circle when viewed from above, namely $d = 2\sqrt{A/\pi}$. Although the rods can be square-like in shape, the main goal was to make a quantitative *comparison* of the uniformity. Hence, one can think of this approximation as simply a numerical step for extracting a characteristic length d from an area A, since the units for length are much more intuitive than the units for area. Standard deviation is quoted rather than variance for this same reason. From the sample set of d, the population standard deviation can be estimated. The absolute variation, as opposed to percent variation, is compared between the images. The SEM images used were all taken at the same magnification of 10000 X, so that the unit length of pixels is common to all of the images.

3.5 Cleaving

The optical characterization of super-collimators requires samples to have straight rows of rods at the edges, in order for light to couple into the devices while minimizing scatter from the roughness. This means that a sample should have at least one freshly-cleaved edge. "Freshly-cleaved" refers to the sample being cleaved during, or close to, the end of the fabrication sequence. In the course of fabrication, a straight row of rods at an edge can be easily damaged during handling or processing.

Wafer cleaving is not an exact science, especially when performed with tweezers and a diamond-tipped pen. The typical silicon wafers used for monitor experiments are spec'ed at a thickness of 525±25 μm. The SOI wafers used for the fabrication of the super-collimators have a thickness of approximately 625 μm. This increase of almost 20% in thickness resulted in a noticeably more difficult cleave for the SOI wafers, which caused rods near the cleaved edges to be dislocated from the substrate due to the weakness of the Si-SiO_2 interface between the 700-nm-tall Si rods (having an aspect ratio[2] of approximately 2.5) and the SiO_2 layer. To prevent the rods from dislodging as shown in Figure 3-28, the samples were cleaved prior to the final RIE step with Cl_2. Prior to the RIE step with Cl_2, the samples consisted of SiO_2 rods on SOI wafer, as shown previously in Figure 3-18. The oxide rods were 120 nm in height (having an aspect ratio of approximately 0.5), and were observed to remain on the substrate at the edge after cleaving.

[2]The aspect ratio for a structure is defined as its height divided by its width.

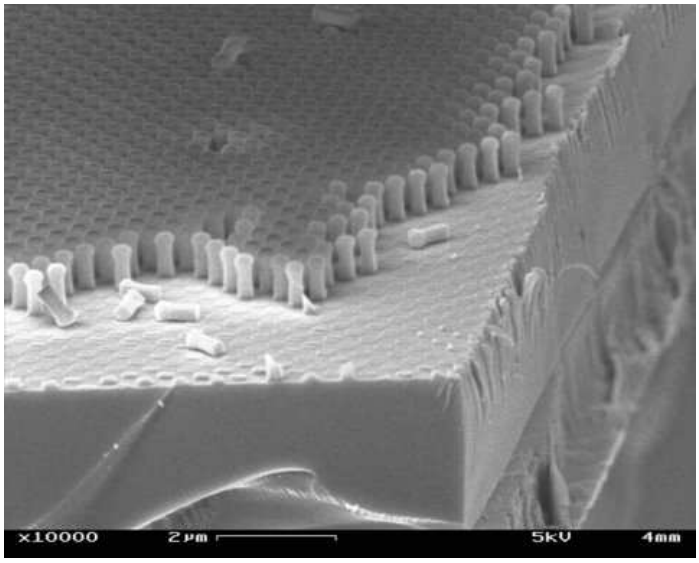

Figure 3-28: The corner of a finished Main Process device at the intersection of 2 cleaves. The rods near the cleaved edges have dislodged due to the nature of the cleaving process.

Chapter 4

Optical Characterization

The super-collimator samples were cleaved into rectangular devices of dimensions between 2 mm and 7 mm on a side. They were then mounted onto a metal holder with crystal-bond wax, and then placed onto a 4-axis stage (position plus tilt angle) in the optical measurement apparatus. Figure 4-1 shows a fabricated super-collimator on its holder.

4.1 Measurement Apparatus

A tunable infrared (IR) laser (wavelength λ ranging from 1260 nm to 1630 nm) is polarized to TM and coupled in-plane into the super-collimator through a high numerical aperture (NA = 0.4) lensed fiber. The lensed fiber's position is piezoelectrically controlled on a 3-axis micropositioning stage. The working distance is 8 μm which results in a spot size of 2.5 μm. The laser power is between 3 and 5 mW. An IR camera and a CCD visible camera are mounted at the opposite facet to aid in the positioning of the lensed fiber relative to the input facet. Another pair of IR and CCD cameras mounted above aids in the positioning of the lensed fiber, as well as captures the top-view of the super-collimator. A schematic of the lab apparatus and a photograph of the same apparatus are shown in Figure 4-2.

The laser wavelength is swept across the range of interest and the top-view IR camera is observed for super-collimation. The scanning program is run from LabView

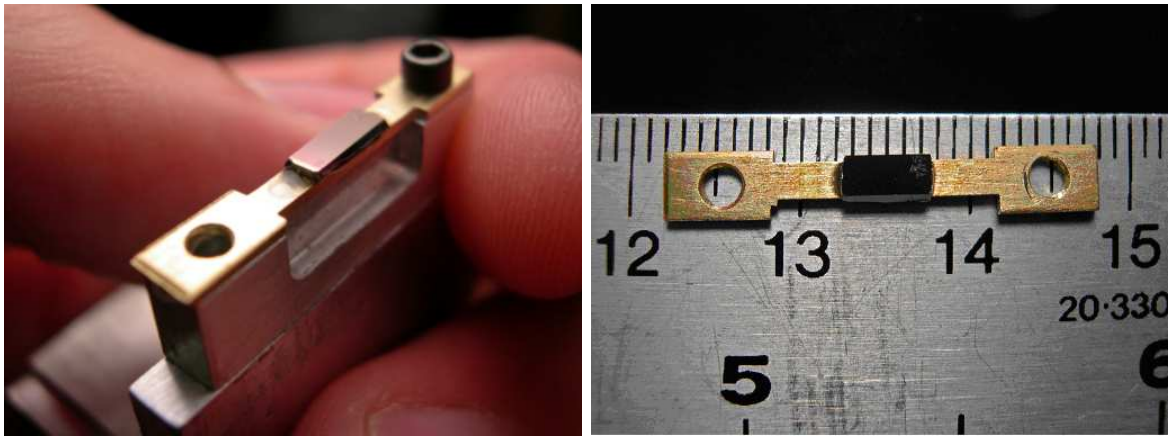

Figure 4-1: One of the device samples resting on its holder. The device size is approximately 2.5 mm by 5 mm.

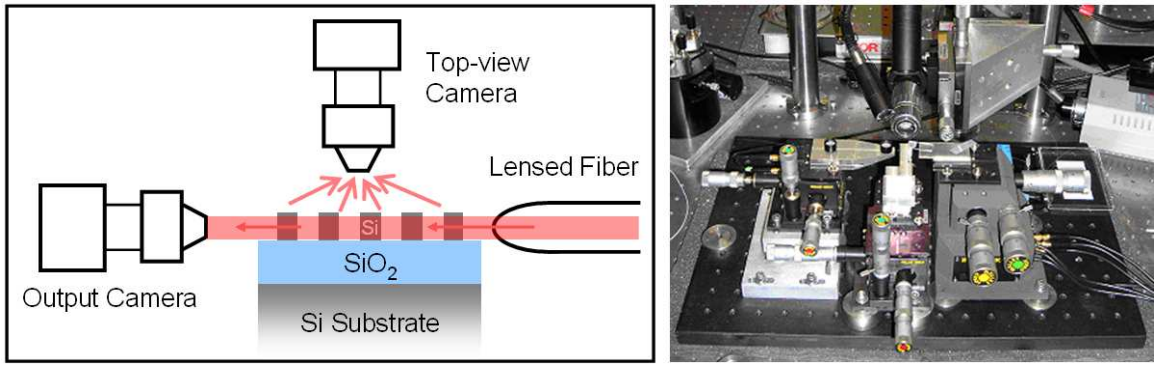

Figure 4-2: Left: schematic of the camera and fiber positions relative to the super-collimator under measurement. Right: photograph of the optical measurement apparatus, which is the same as the one used for measuring super-collimation in [1].

(made by National Instruments). Characterization was performed by Marcus Dahlem (advised by Erich Ippen) in the Optics and Quantum Electronics Group.

4.2 Results and Discussion

Super-collimation was observed with the top-view IR camera, which captures scattered light due to imperfections in the PhC. Figure 4-3 is such an IR image[1] at a wavelength of $\lambda = 1545$ nm, close to the target wavelength of 1550 nm. The spot at

[1] All of the IR images shown are averages of 300 separate images taken at wavelengths differing by 0.01 nm around the reported central wavelength. This technique is used to reduce noise due to laser speckle [25].

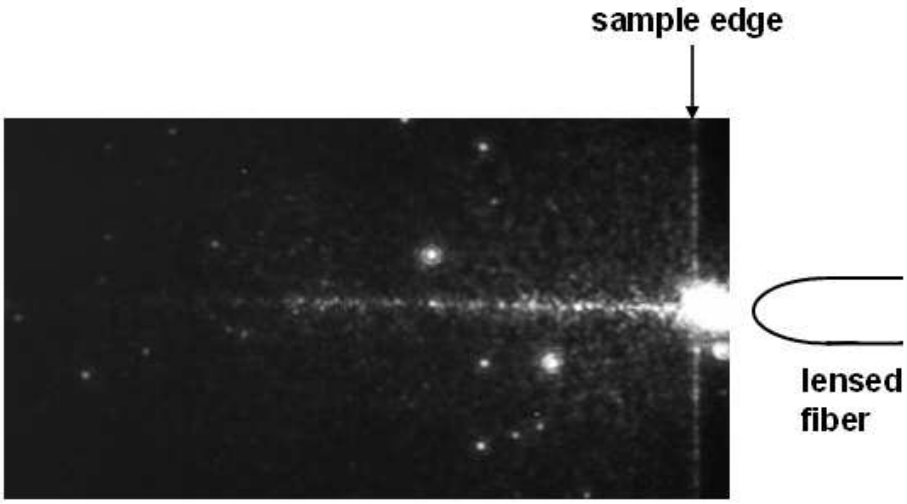

Figure 4-3: Super-collimation observed at a wavelength of $\lambda = 1545$ nm. The image is approximately 250 μm wide.

the right side of the image is the scattering caused as the laser beam enters the PhC. The coupling efficiency is about 15%.

Figure 4-4 shows spreading of the light beam in the super-collimator as the wavelength is changed. This particular sample super-collimated at a wavelength of near 1530 nm. Changing the wavelength corresponds to operating on different equifrequency contour lines. At the super-collimation wavelength, the equifrequency contour line is flat, but at neighboring wavelengths the equifrequency contour lines will have slight curvatures, resulting in the noticeable spreading.

Recall that the rods are tapered and not cylindric as designed. The diameters of the top and bottom of the rods can be estimated from side-view SEM images to be approximately 228 nm and 285 nm, respectively. The average diameter is then 256.5 nm, which is very close to the diameter of the designed cylindrical rods. Simulations confirm that the super-collimation wavelength of the tapered rods can be estimated by the super-collimation wavelength of cylindrical rods at the average tapered diameter. Different super-collimation wavelengths were observed for difference device samples, probably due to slight differences in the fabrication of the separate samples.

Figure 4-5 shows a super-collimating beam at a wavelength of 1550 nm propagating at least 350 μm in the sample, a distance that is more than 25 times the isotropic

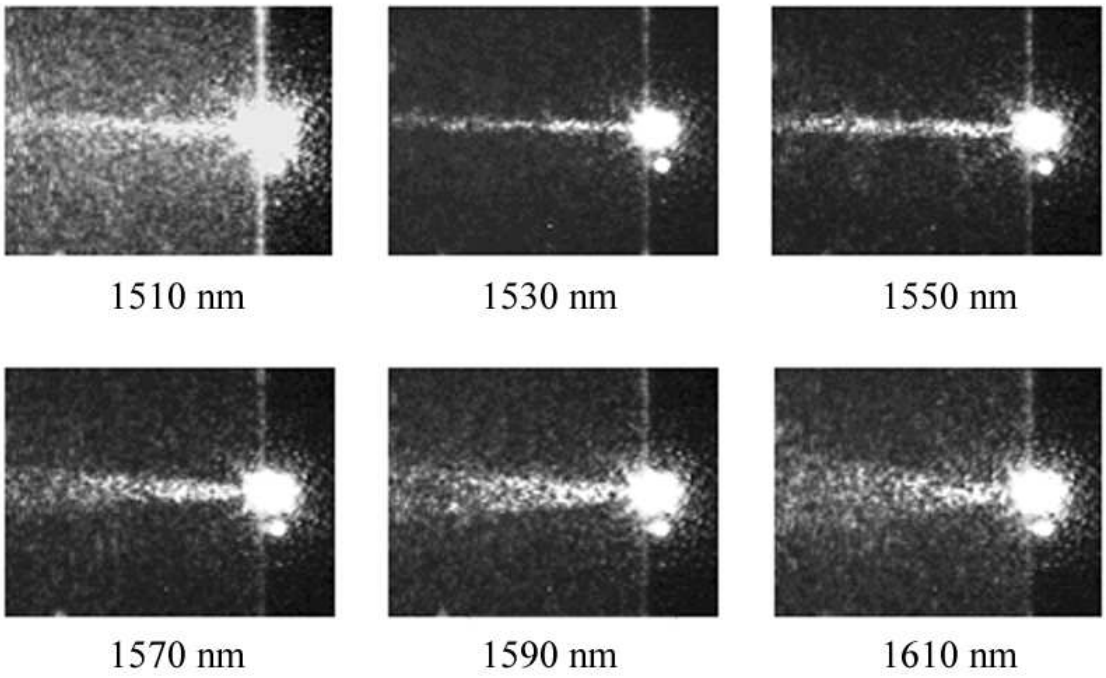

Figure 4-4: The divergence of the beam as a function of wavelength is seen clearly in the set of top-view IR images. Each image is approximately 125 μm wide. Super-collimation occurs close to $\lambda = 1530$ nm.

diffraction-length. The isotropic diffraction length L_d is a metric for the scale of collimation, defined as the distance over which a Gaussian optical beam would normally spread by a factor of $\sqrt{2}$ in an isotropic medium. L_d is found by the formula $L_d = \pi w^2/\lambda$, where w is the Gaussian beam waist radius and λ is the wavelength of light in the direction of propagation. At a wavelength of 1550 nm with a spot size of 2.5 μm, $L_d = 12.7$ μm. To the best of the author's knowledge, with the exception of the previous super-collimation work at MIT [1], this is the longest experimental demonstration of super-collimation in an optical 2D PhC device to date. It is also, to the author's best knowledge, the first experimental demonstration of super-collimation in a rod-based PhC device.

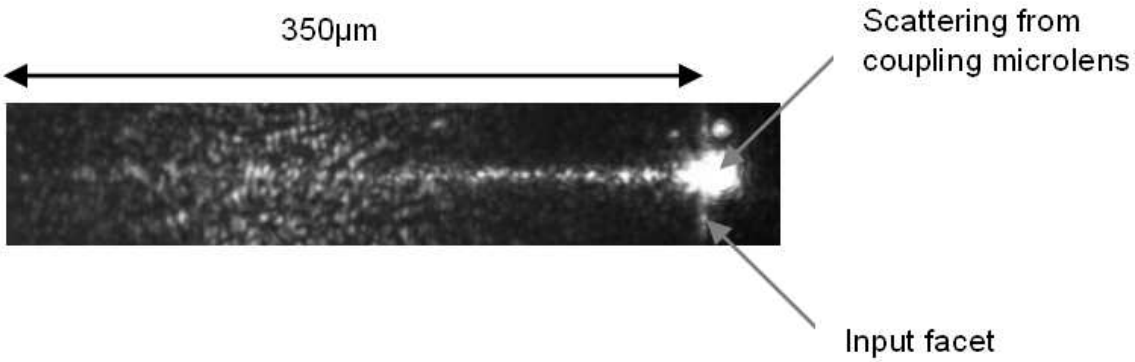

Figure 4-5: Demonstration of super-collimation for a distance of at least 350 μm at $\lambda = 1550$ nm.

Chapter 5

Conclusion

The work presented in the thesis included the design, fabrication, and characterization of a rod-based 2D photonic crystal super-collimator. The dispersion contours for the PhC were simulated during the design process. Two different fabrication methods were developed and applied. The super-collimator was fabricated, and the fabrication methods were analyzed and compared. Characterization of the super-collimator resulted in the first experimental observation of super-collimation in a 2D PhC of rods.

5.1 Applications and Future Work

Super-collimation has been seen as an important tool in the development of integrated optical circuits. Designs for optical routing and optical logic utilizing super-collimation have been developed [4]. Photonic crystals exhibit many useful properties other than super-collimation, and optical logic chips with integrated photonic crystal structures can be envisioned for the future. Interfacing between traditional waveguides and PhCs is already under investigation [26, 27].

Most of the optical logic today is achieved with optical and/or electrical signals. In other words, the optical properties of a component are altered with photons or voltages. Certainly, this is needed for high-speed applications. However, more recently, lower-speed applications in which the optical properties of a component are

changed with fluids are receiving interest as well. This is the field of optofluidics, the integration of optics and photonics with micro- and nano-fluidics [28].

Two-dimensional PhCs of holes have been experimentally shown to be tunable via hole-filling with different liquids [29]. The propagation of light through a PhC is changed when there is a liquid present between the dielectric structures. In a 2D PhC of air-holes, however, the fluid must be made to either flow above the PhC holes and parallel to the PhC plane [30], or through the holes but perpendicular to the PhC plane in a PhC fiber [31]. In rod-based PhCs, however, fluids can flow both through (between) the PhC rods and parallel to the PhC plane, opening new doors for applications (see Figure 5-1).

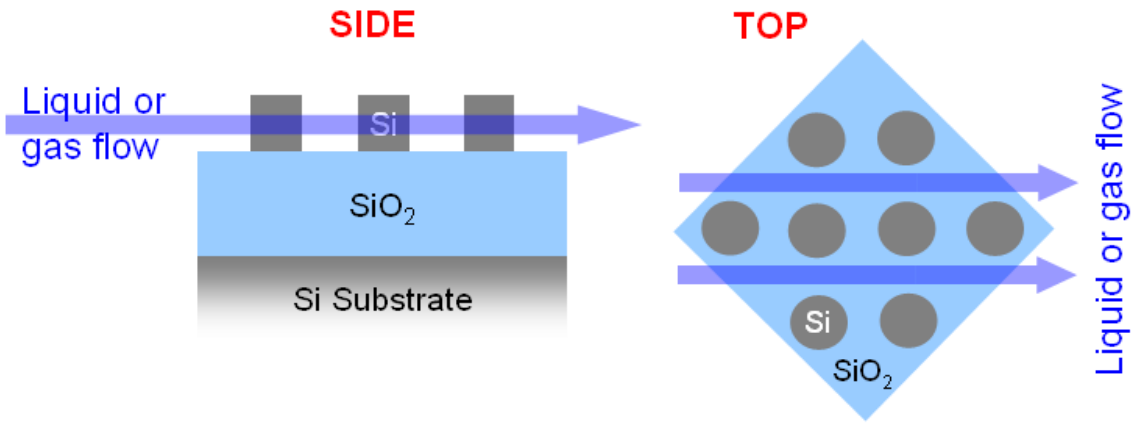

Figure 5-1: In a 2D PhC of rods, fluid can flow parallel to the PhC plane between the rods.

A sensing platform based on a 2D PhC super-collimator of rods is one potential application. For example, a protein detection system has been developed with a 2D PhC of holes by utilizing defect-based waveguiding [32]. However, a rod-based geometry is believed to provide a better foundation for such a sensor. Rod-based PhCs allow for in-plane fluid flow through the PhC. Furthermore, rod-based super-collimators have a 6-fold increase in sensitivity over hole-based super-collimators to the ambient chemical composition, as discussed in Section 2.4.

Figure 5-2 is a simplified schematic of a possible sensor design. The super-collimation wavelength is a function of the refractive indices of the dielectric rods and

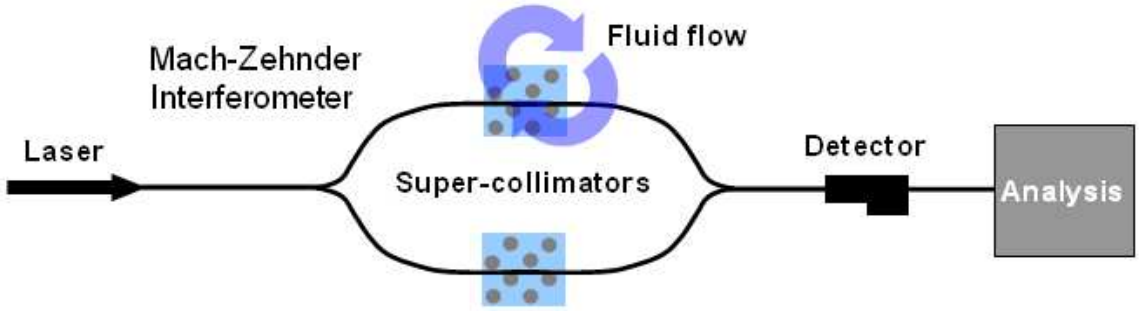

Figure 5-2: A possible chemical sensor structure based on a Mach-Zehnder design utilizing super-collimating 2D PhCs of rods.

the medium between the rods. Propagation through the super-collimator is changed when there is a chemical present between the dielectric rods. The change will result in a phase shift between the two arms, which can be used to determine the identity of the chemical of interest. Photonic crystal chemical sensors will be able to measure gas or liquid species, and provide immediate analysis of the properties of the chemicals.

The short-term goals for this project include further investigation into potential applications in the area of optofluidic integration, akin to the sensor design described above. Characterization of the fabricated super-collimator will also continue, in an effort to gain a better understanding of super-collimation. The long-term goals include research on other 2D and 3D photonic crystals, as well as other types of metamaterials. The design, fabrication, characterization, and application of these devices are of interest.

Appendix A

Tables

Table A.1: Refractive indices of relevant materials. Adapted from [17].

Material	**n (325 nm)**
Chromium	1.12 - i2.95
Silicon	4.68 - i2.03
SiO_2	1.48
BARLi	1.55 - i0.14
PFI-88	1.79 - i0.02
PS4	1.681 - i0.016

Table A.2: Spin-coating parameters

Layer	**Thickness**	**Spin Speed**	**Softbake**
BARLi	286 nm	3.1 krpm	175°C, 90 s
BARLi	400 nm	1.6 krpm	175°C, 90 s
PS4	200 nm	3.3 krpm	90°C, 90 s
PFI-88	200 nm	3.8 krpm	90°C, 90 s

Table A.3: Lift-off Process RIE parameters

Layer	SiO_2	BARLi	Si
Gas(es)	CF_4	He/O_2	CF_4/O_2
Flow (sccm)	15	10/5	13.5/1.5
Pressure (mT)	10	7	10
Power (W)	150	142	155
Voltage (V)	330	250	48
Time (min:sec)	1:10	6:50	40:00
Etch Rate (nm/min)	20	60	17.5

Table A.4: Main Process RIE parameters

Layer	SiO_2 Interlayer	BARLi	Si Hardmask	BARLi Strip	Si
Gas(es)	CF_4	He/O_2	CF_4	He/O_2	Cl_2
Flow (sccm)	15	10/5	15	10/5	13
Pressure (mT)	10	7	10	7	4.5
Power (W)	148	150	148	152	88
Voltage (V)	314	244	301	244	514
Time (min:sec)	1:05	5:00	6:20	5:00	10:00
Etch Rate (nm/min)	20	60	20	60	70

Table A.5: "Outerlab" clean/condition process RIE parameters

Step	**Gas(es)**	**Flow (sccm)**	**Pressure**	**Power**	**Voltage**	**Time (min:sec)**
1	CF_4/O_2	10.8/23.8	36 mT	60 W	312-292 V	60:00
2	CHF_3/O_2	16.2/4.1	11 mT	30 W	250 V	20:00
3	Cl_2	13	11 mT	90 W	420 V	4:00

References

[1] P. Rakich, M. Dahlem, S. Tandon, M. Ibanescu, M. Soljačić, G. Petrich, J. Joannopoulos, L. Kolodziejski, and E. Ippen. Achieving centimetre-scale supercollimamtion in a large-area two-dimensional photonic crystal. *Nature Materials*, 5:93, 2006.

[2] L. Wu, M. Mazilu, and T. Krauss. Beam steering in planar-photonic crystals: from superprism to supercollimator. *Lightwave Technology, Journal of*, 21(2):561–566, 2003.

[3] Sheila N. Tandon. *Engineering Light Using Large Area Photonic Crystal Devices*. PhD thesis, Cambridge, MA, 2005.

[4] D.W. Prather, S. Shi, J. Murakowski, G.J. Schneider, A. Sharkawy, C. Chen, B.L. Miao, and R. Martin. Self-collimation in photonic crystal structures: a new paradigm for applications and device development. *Journal of Physics D: Applied Physics*, 40(9):2635–2651, 2007.

[5] John D. Joannopoulos, Robert D. Meade, and Joshua N. Winn. *Photonic Crystals*. Princeton University Press, 1995.

[6] H. Kosaka, T. Kawashima, A. Tomita, M. Notomi, T. Tamamura, T. Sato, and S. Kawakami. Superprism phenomena in photonic crystals. *Physical Review B*, 58(16):10096–10099, 1998.

[7] S. Tandon, M. Soljacic, G. Petrich, J. Joannopoulos, and L. Kolodziejski. The superprism effect using large area 2D-periodic photonic crystal slabs. *Photonics and Nanostructures–Fundamentals and Applications*, 3:10–18, 2005.

[8] H. Kosaka, T. Kawashima, A. Tomita, M. Notomi, T. Tamamura, T. Sato, and S. Kawakami. Self-collimating phenomena in photonic crystals. *Applied Physics Letters*, 74:1212, 1999.

[9] S. Kawakami. Fabrication of submicrometre 3D periodic structures composed of Si/SiO_2. *Electronics Letters*, 33(14):1260–1261, 1997.

[10] X. Yu and S. Fan. Bends and splitters for self-collimated beams in photonic crystals. *Applied Physics Letters*, 83(16):3251, 2003.

[11] D.W. Prather, S. Shi, D.M. Pustai, C. Chen, S. Venkataraman, A. Sharkawy, G.J. Schneider, and J. Murakowski. Dispersion-based optical routing in photonic crystals. *Optics Letters*, 29(1):50–52, 2004.

[12] J.D. Joannopoulos and S.G. Johnson. *Photonic Crystals: The Road from Theory to Practice*. Kluwer Academic Pub, 2002.

[13] S. Johnson and J. Joannopoulos. Block-iterative frequency-domain methods for Maxwell's equations in a planewave basis. *Optics Express*, 8(3):173–190, 2001.

[14] K.M. Ho, C.T. Chan, and C.M. Soukoulis. Existence of a photonic gap in periodic dielectric structures. *Physical Review Letters*, 65(25):3152–3155, 1990.

[15] R.D. Meade, A.M. Rappe, K.D. Brommer, J.D. Joannopoulos, and O.L. Alerhand. Accurate theoretical analysis of photonic band-gap materials. *Physical Review B*, 48(11):8434–8437, 1993.

[16] Luxpop thin film and bulk index of refraction and photonics calculations. http://luxpop.com.

[17] Michael E. Walsh. *On the Design of Lithographic Interferometers and their Application*. PhD thesis, Cambridge, MA, 2004.

[18] Maya S. Farhoud. *Fabrication and Characterization of Nanostructured Magnetic Particles for Applications in Data Storage*. PhD thesis, Cambridge, MA, 2001.

[19] Sheila N. Tandon. Design and fabrication of a superprism using 2d photonic crystals. Master's thesis, Cambridge, MA, 2002.

[20] J.W. Coburn. *Plasma Etching and Reactive Ion Etching*. American Institute of Physics, 1982.

[21] R. d'Agostino, F. Cramarossa, S. De Benedictis, and G. Ferraro. Spectroscopic diagnostics of CF_4-O_2 plasmas during Si and SiO_2 etching processes. *J. Appl. Phys*, 52(3), 1981.

[22] T. C. Garza, P. Lozano, L. F. Velasquez-Garcia, and M. Martinez-Sanchez. Black silicon treatments to improve silicon wettability for use in electrospray propulsion.

[23] H.S. Hoffman. *Statistics Explained: A Computer Assisted Guide to the Logic of Statistical Reasoning*. University Press of America, 1985.

[24] K.P. Giapis, G.R. Scheller, R.A. Gottscho, W.S. Hobson, and Y.H. Lee. Microscopic and macroscopic uniformity control in plasma etching. *Applied Physics Letters*, 57:983, 1990.

[25] Marcus Dahlem. Optical studies of super-collimation in photonic crystals. Master's thesis, Cambridge, MA, 2005.

[26] H. Kosaka, T. Kawashima, A. Tomita, T. Sato, and S. Kawakami. Photonic-crystal spot-size converter. *Applied Physics Letters*, 76:268, 2000.

[27] S. Assefa, P.T. Rakich, P. Bienstman, S.G. Johnson, G.S. Petrich, J.D. Joannopoulos, L.A. Kolodziejski, E.P. Ippen, and H.I. Smith. Guiding 1.5 μm light in photonic crystals based on dielectric rods. *Appl. Phys. Lett*, 85(25):6110–6112, 2004.

[28] D. Psaltis, S.R. Quake, and C. Yang. Developing optofluidic technology through the fusion of microfluidics and optics. *Nature*, 442(7101):381–6, 2006.

[29] D. Erickson, X. Heng, Z. Li, T. Rockwood, T. Emery, Z. Zhang, A. Scherer, C. Yang, and D. Psaltis. Optofluidics. *Proceedings of SPIE*, 5908:59080S, 2005.

[30] D. Erickson, T. Rockwood, T. Emery, A. Scherer, and D. Psaltis. Nanofluidic tuning of photonic crystal circuits. *Optics Letters*, 31(1):59–61, 2006.

[31] P. Domachuk, H.C. Nguyen, B.J. Eggleton, M. Straub, and M. Gu. Microfluidic tunable photonic band-gap device. *Applied Physics Letters*, 84:1838, 2004.

[32] M.R. Lee and P.M. Fauchet. Two-dimensional silicon photonic crystal based biosensing platform for protein detection. *Optics Express*, 15(8):4530–4535, 2007.